UNIVERSITY OF HELSINKI REPORT SERIES IN PHYSICS

HU-P-D183

NANOSCALE STUDIES OF MATERIALS USING X-RAY SYNCHROTRON RADIATION AND MESOSCOPIC MODELLING

Kari Pirkkalainen

Division of Materials Physics
Department of Physics
Faculty of Science
University of Helsinki
Helsinki, Finland

ACADEMIC DISSERTATION

To be presented, with the permission of
the Faculty of Science of the University of Helsinki,
for public criticism in Auditorium D101
of the Department of Physics (Physicum),
Gustaf Hällströmin katu 2a, on September 9th 2011 at 12:15

Helsinki 2011

Supervisors:

Prof. Ritva Serimaa
Department of Physics
University of Helsinki
Helsinki, Finland

Dr. Ismo T. Koponen
Department of Physics
University of Helsinki
Helsinki, Finland

Pre-examiners:

Prof. Tapio Ala-Nissilä
Department of Applied Physics
Aalto University School of Science and Technology
Espoo, Finland

Dr. Reidar Lund
Center for Material Physics (CFM)
University of the Basque Country
San Sebastian, Spain

Opponent:

Prof. Jan Skov Pedersen
Department of Chemistry
Aarhus University
Aarhus, Denmark

Custos:

Prof. Ritva Serimaa
Department of Physics
University of Helsinki
Helsinki, Finland

Report Series in Physics HU-P-D183
ISSN 0356-0961
ISBN 978-952-10-6883-6 (printed version)
ISBN 978-952-10-6884-3 (pdf version)
http://ethesis.helsinki.fi/
Helsinki University Print
Helsinki 2011

Preface

This thesis is based on research done at the Div. of Materials Physics and Div. of Geophysics and Astronomy (Dept. of Physics, Univ. of Helsinki), at the Finnish Forest Research Institute, at the European Synchrotron Radiation Facility (Grenoble, France), at the Deutsches Elektronen-Synchrotron (Hamburg, Germany), at the Dept. of Applied Physics (Aalto University), and at the Institute of Macromolecular Compounds (Russian Academy of Sciences, St. Petersburg, Russia). I acknowledge all the researchers whom I have had the privilige to collaborate with. Prof. Juhani Keinonen is acknowledged for providing me the opportunity to work at the Dept. of Physics.

First and foremost I wish to thank my supervisors Prof. Ritva Serimaa and Doc. Ismo T. Koponen. Prof. Serimaa gave me a chance to work as an undergraduate summer student in 2005 under her supervision in the (former) x-ray laboratory. After that I have had the privilige to work in her soft-matter related group for the duration of my graduate studies. I have especially enjoyed working as a teaching assistant in her advanced undergraduate courses, including the *Soft-condensed matter physics* and *Synchrotron radiation in materials research*. In addition, her participation to evening programmes on various conferences, beam-line experiments, and summer schools has been exemplary, and has really brought her more approachable to the students.

Doc. Koponen I commend on his wits and charm. I have never had so much fun discussing the intricate details of theoretical physics. The combination of good humour, easygoing attitude and quick-thinking makes him a wonderful person to be around with. Respect!

I wish to thank the former and current researchers of the Division of Materials Physics. You are all awesome! The general atmosphere in the lab is friendly, positive and encouraging, and for this I acknowledge Prof. Keijo Hämäläinen who has been essential in creating and maintaining this atmosphere. I want to specially thank Dr. Ulla Vainio for tutoring me (and perhaps even believing in me?!) in the early stages of my studies, Kirsi Leppänen for various collaborations and discussions, and Arto Sakko for fruitful discussions on life, universe and everything. The lab Christmas party band ("The Hard X-rays" or "Paavo and the perverts"), including me, Iina, Paavo, Tuomas and Käpy, is very much appreciated and always remembered. Last but not the least, the lab floorball team has provided me with a great way to relieve frustration and stress. The weekly floorball games have made the road to this thesis a little bit less bumpier. I really hope you continue these great traditions after I have moved on.

NGS-NANO (National Doctoral Programme in Nanoscience) is acknowledged for funding my graduate studies and making it possible to meet other researchers in various summer schools and meetings.

Helsinki, 19th of April, 2011, Kari Pirkkalainen

K. Pirkkalainen: Nanoscale studies of materials using x-ray synchrotron radiation and mesoscopic modelling, University of Helsinki, 2011, 47 pages + appendices.
University of Helsinki, Report Series in Physics, HU-P-D183

Classification (INSPEC): A6110F, A6146, A6185
Keywords: synchrotron radiation, x-ray diffraction, EXAFS, cellulose, nanoparticle, nucleation & growth, size-selection

Abstract

X-ray synchrotron radiation was used to study the nanostructure of cellulose in Norway spruce stem wood and powders of cobalt nanoparticles in cellulose support. Furthermore, the growth of metallic clusters was modelled and simulated in the mesoscopic size scale.

Norway spruce was characterized with x-ray microanalysis at beamline ID18F of the European Synchrotron Radiation Facility in Grenoble. The average dimensions and the orientation of cellulose crystallites was determined using x-ray microdiffraction. In addition, the nutrient element content was determined using x-ray fluorescence spectroscopy. Diffraction patterns and fluorescence spectra were simultaneously acquired.

Cobalt nanoparticles in cellulose support were characterized with x-ray absorption spectroscopy at beamline X1 of the Deutsches Elektronen-Synchrotron in Hamburg, complemented by home lab experiments including x-ray diffraction, electron microscopy and measurement of magnetic properties with a vibrating sample magnetometer. Extended x-ray absorption fine structure spectroscopy (EXAFS) and x-ray diffraction were used to solve the atomic arrangement of the cobalt nanoparticles. Scanning- and transmission electron microscopy were used to image the surfaces of the cellulose fibrils, where the growth of nanoparticles takes place. The EXAFS experiment was complemented by computational coordination number calculations on ideal spherical nanocrystals.

The growth process of metallic nanoclusters on cellulose matrix is assumed to be rather complicated, affected not only by the properties of the clusters themselves, but essentially depending on the cluster-fiber interfaces as well as the morphology of the fiber surfaces. The final favored average size for nanoclusters, if such exists, is most probably a consequence of these two competing tendencies towards size selection, one governed by pore sizes, the other by the cluster properties. In this thesis, a mesoscopic model for the growth of metallic nanoclusters on porous cellulose fiber (or inorganic) surfaces is developed. The first step in modelling was to evaluate the special case of how the growth proceeds on flat or wedged surfaces.

List of publications

This thesis consists of an introductory part followed by five publications, which are referred to by Roman numerals **I-V** throughout the text.

I K. Pirkkalainen, M. Peura, K. Leppänen, A. Salmi, A. Meriläinen, P. Saranpää, R. Serimaa, *Simultaneous x-ray diffraction and x-ray fluorescence microanalysis on secondary xylem of Norway spruce*, submitted to Wood Sci. Technol.

II K. Pirkkalainen, K. Leppänen, U. Vainio, M.A. Webb, T. Elbra, T. Kohout, A. Nykänen, J. Ruokolainen, N. Kotelnikova, R. Serimaa, *Nanocomposites of magnetic cobalt nanoparticles and cellulose*, Eur. Phys. J. D **49** (2008), 333-342.

III K. Pirkkalainen, R. Serimaa, *Coordination number in ideal spherical nanocrystals*, J. Appl. Cryst. **42** (2009), 442-447.

IV K. Pirkkalainen, K.A. Riekki, I.T. Koponen, *Two computational methods for describing size selected nanocluster growth and obtaining accurate cluster size distributions*, Comp. Mat. Sci **43** (2008), 325-336.

V K. Pirkkalainen, I.T. Koponen, *Computational study on tuning the 2D self assembly of metallic nanoclusters*, Surf. Sci. **604** (2010), 951-956.

The research papers **I-V** are included as appendices in the printed version of this thesis and they are reprinted with permission from the publishers.

Author's contribution

Paper I

K.P. participated in planning and performing the x-ray microanalysis measurements at beamline ID18F in ESRF, Grenoble. He was also responsible for the data analysis and writing of the paper. Sample material was obtained from the Finnish Forest Research Institute by the courtesy of P. Saranpää.

Paper II

K.P. participated in planning and performing the x-ray absorption spectroscopy measurements at beamline X1 in DESY, Hamburg. The quantitative EXAFS analysis was done by K. Leppänen. X-ray diffraction measurements and data analysis were done jointly by K.P. and K. Leppänen. Electron microscopy studies were done by K. Leppänen and A. Nykänen and vibrating sample magnetometer measurements by K. Leppänen, T. Kohout and T. Elbra. The results were compiled jointly by K.P. and K. Leppänen. The paper was mostly written by K.P., with other authors providing comments and corrections to the text. The sample powders were obtained from the Institute of Macromolecular Compounds, Russian Academy of Sciences, St. Petersburg by the courtesy of N. Kotelnikova.

Paper III

K.P. was responsible for simulations, data analysis and writing the paper. R. Serimaa provided valuable comments and corrections at all stages of the study.

Paper IV

K.P. was responsible for practical implementation of the MED simulation method, data analysis related to it, writing about 1/3 of the paper and editing the final version of the paper. K.A. Riekki did all the PCM simulations and the data analysis related to it, and also wrote the parts concerning PCM; I.T. Koponen was the mastermind and was also responsible for the theoretical aspects of the study.

Paper V

K.P. was responsible for all the simulations, data analysis and writing the paper. I.T. Koponen wrote some parts of the paper and provided valuable insight, comments and corrections at all stages of the study.

Other related work

List of work by the author that is closely related to this thesis but not included in it. The list was updated on the 4th of July, 2011.

- J. Stevanic, C. Joly, K.S. Mikkonen, K. Pirkkalainen, R. Serimaa, C. Rémond, M. Tenkanen, L. Salmén, *Bacterial nanocellulose-reinforced arabinoxylan films*, J. Appl. Pol. Sci. (2011), E-pub. ahead of print, DOI: 10.1002/app.34217.

- E. Kontturi, M. Suchy, P.A. Penttilä, B. Jean, K. Pirkkalainen, M. Torkkeli, R. Serimaa, *Amorphous Characteristics of an Ultrathin Cellulose Film*, Biomacromolecules **12** (2011), 770-777.

- K.S. Mikkonen, J. Stevanic, C. Joly, P. Dole, K. Pirkkalainen, R. Serimaa, L. Salmén, M. Tenkanen, *Composite films from spruce galactoglucomannans with microfibrillated spruce wood cellulose*, Cellulose **18** (2011), 713-726.

- K.S. Mikkonen, A.P. Matthew, K. Pirkkalainen, R. Serimaa, C. Xu, S. Willfor, K. Oksman, M. Tenkanen, *Glucomannan composite films with cellulose nanowhiskers*, Cellulose (2010) **17**, 69-81.

- O.M. Feroughi, C. Sternemann, C.J. Sahle, M.A. Schroer, H. Sternemann, H. Conrad, A. Hohl, G.T. Seidler, J. Bradley, T.T. Fister, M. Balasubramanian, A. Sakko, K. Pirkkalainen, K. Hämäläinen, M. Tolan, *Phase separation and Si nanocrystal formation in bulk SiO studied by x-ray scattering*, Appl. Phys. Lett. **96** (2010), 081912.

- K. Leppänen, K. Pirkkalainen, P.A. Penttilä, J. Sievänen, N.E. Kotelnikova, R. Serimaa, *Small-angle x-ray scattering study on the structure of microcrystalline and nanofibrillated cellulose*, J. Phys. Conf. Ser. **247** (2010), 012030.

- N.E. Kotelnikova, E.L. Lysenko, R. Serimaa, K. Pirkkalainen, U. Vainio, V.K. Lavrentev, D.A. Medvedeva, A.L. Shakhmin, N.N. Saprykina, N.P. Novolelov, *Cellulose as a nanoreactor for the synthesis of nickel nanoparticles*, Polym. Sci. Ser. A Polym. Phys. **50** (2008), 51-57.

- U. Vainio, K. Pirkkalainen, K. Kisko, G. Goerigk, N.E. Kotelnikova, R. Serimaa, *Copper and copper oxide nanoparticles in a cellulose support studied using anomalous small-angle x-ray scattering*, Eur. Phys. J. D **42** (2007), 93-101.

- K. Pirkkalainen, U. Vainio, K. Kisko, T. Elbra, T. Kohout, N.E. Kotelnikova, R. Serimaa, *Structure of nickel nanoparticles in a microcrystalline cellulose matrix studied using anomalous small-angle X-ray scattering*, J. Appl. Cryst. **40** (2007), 489-494.

Contents

1 Introduction

In his famous lectures, Richard Feynman said that "all things are made of atoms" [1]. This was very well said and certainly true, but I would like to add that "all practical things are made of aggregates of atoms". As it turns out, the size of an aggregate, i.e. how many atoms it consists of, is a convenient way to define the aggregate. In the following, I will indicate that aggregates of atoms in all size scales are important. The definitions given here are only suggestive, and the reader will find various classifications from other sources [2] [3, Ch. 2]. In the field of nanoscience the basic unit of length is the nanometer (nm), which is equal to one billionth of a meter (1 nm = 10^{-9} m). 1000 nanometers is equal to 1 micrometer (μm). However, in x-ray physics the Ångström 1 Å = 0.1 nm = 10^{-10} m) is often preferred due to the fact that the wavelength of electromagnetic radiation produced by x-ray tubes is about 1 Å [4].

The bonding of two or a few atoms (or ions) makes molecules. The most important simple molecules for our existence are oxygen (O_2) and water (H_2O). Considerably larger and more complex molecules are termed (bio)macromolecules or (bio)polymers. The prefix "bio" is used if the aggregate in question can be associated with living things. All currently known life forms are "constructed" according to the coded information in a biomacromolecule known as the DNA. One of the most common man-made polymer is polyethylene (PE), which is the material plastic bags are made of. An example of a naturally occurring polymer is cellulose, which is produced in abundance by e.g. plants. As it happens, the atomic scale structure of DNA [5], PE [6, 7] and cellulose [8] have all been determined by x-ray diffraction which plays an important role in this thesis also.

Aggregates of about 20 or more atoms, but smaller than about 1 nm in all dimensions, can be called clusters or nanoclusters. If the size of the aggregate is larger than 1 nm and smaller than 100 nm, it is often called a nanoparticle. Perhaps the most distinct feature of nanoparticles/clusters is the size effect : the dimensions of the aggregate have a profound effect on its properties [9, 10]. In addition to the size effect, the properties are dependent e.g. on the shape of the particle, distances between neighboring particles and the medium where the particles are dispersed. [2, 11–13]

Nanoparticles can be divided into different categories depending on their physical properties. In case of electrical properties, there are metallic and semiconducting nanoparticles [3, Ch. 2] [10], and in case of magnetic properties, there are ferromagnetic (including ferri- and antiferromagnetic), paramagnetic and diamagnetic nanoparticles [2] [14, Chs. 1&6]. Nanoparticles with very distinct discrete electronic energy levels are termed quantum dots.

Aggregates of atoms much larger than 100 nanometers in all dimensions have properties that often resemble those observed in bulk materials. If the aggregate of atoms is a bulk solid, there is no size-effect, i.e. increasing the size of the aggregate further

does not alter its chemical or physical properties in a discernible way.

Nanoparticles are the first category of nanostructured materials (NsM), which is a category encompassing all materials with microstructural components of the size of few nanometers. The second category of NsM comprises bulk material with nanometer-sized surface features i.e. epitaxially grown thin surface layers, islands and wires. The third category are bulk solids with a nanometer-scale microstructure e.g. polycrystalline materials with very small grain sizes. [11, 12]

The practical importance of nanostructured materials is obvious. For example the advent of personal computers can very well be attributed to the advances in magnetic storage, which are due to the discovery of giant magnetoresistance (GMR) by the Nobel Prize winners of 2007, Albert Fert and Peter Grünberg (see the original papers [15, 16]). The GMR components are actually nanostructured materials with repeating ferromagnetic and antiferromagnetic thin layers. The nature is full of nanoparticles e.g. in the human brain, in flora and fauna, in the soil of Earth and in interstellar space [14, Ch. 1]. Potential medical applications include intercellular biosensors, precise drug delivery and hyperthermia agents against tumors [14, Ch. 10].

Due to their small size as compared to the wavelength of optical light (ca. 400-800 nm), the characterization of nanoparticles is beyond the capabilities of the human eye, or of microscopic techniques relying on the same region of electromagnetic spectrum. The obvious solution is to lower the wavelength of the probe to about 0.1 nm, which corresponds to electromagnetic radiation in the x-ray region. Unfortunately the direct real space imaging of nanoscale structures with x-rays is at the moment limited by the inadequate quality of x-ray lenses. As a consequence, the characterization of materials with x-rays is an indirect method of obtaining structural information. For example the x-ray diffraction pattern is essentially a projection image of the reciprocal space of the electron density in the measured sample, and in extended x-ray absorption fine structure spectroscopy the obtained oscillatory pattern is a reciprocal space representation of the average radial density function around a given atom species. The resolution to real space information requires the utilization of Fourier analysis, and either prior knowledge or good educated guesswork about the studied nanostructure. [4, 17, 18]

The recent advances in experimental characterization techniques are making it possible to study the growth of nanoclusters *in situ*. For example, at the advent of novel x-ray based probes using either modern synchrotrons or x-ray free electron lasers, the spatial and temporal resolution for nanocluster growth studies is practically in our reach. In order to explain some of the phenomena occuring at the nucleation and growth stages, modelling is required. Therefore, the modelling of nucleation and growth of nanoclusters theoretically and computationally has never been more topical.

2 The aim of the study

The main focus of this thesis is not the potential application of nanostructured materials, or their novel electronic and magnetic properties. Instead, the focus is on the structural aspects of nanoparticles and the characterization of these structures by x-ray based experimental methods (papers **I** and **II**).

The composition, crystal structure, crystallinity, and grain sizes of nanoparticles are characterized by x-ray diffraction (XRD). The average chemical neighborhood of atoms in well-ordered and disordered nanoparticles is revealed by extended x-ray absorption fine structure (EXAFS) spectroscopy. The atomic elements present in nanoparticles are found by x-ray fluorescence spectroscopy (XRF). In most cases, the experiments are done using high brilliance x-ray synchrotron radiation available in modern synchrotrons such as HASYLAB in Hamburg, Germany, and ESRF in Grenoble, France.

In addition to the x-ray based experiments, several complementary characterization methods were used e.g. optical microscopy (OM), scanning and transmission electron microscopy (SEM and TEM), and magnetic measurements using a vibrating sample magnetometer (VSM). Although these methods are in an important role in papers **I** and **II**, they are not discussed further in the introductory part of the thesis.

The experimentally studied materials include nanocomposites of cobalt nanoparticles in microcrystalline cellulose support (paper **II**), and nanocrystallites of cellulose in Norway spruce wood (paper **I**). These can both be included into the first category of nanostructured materials: supported or embedded nanometer sized-particles. The cobalt nanoparticles are especially interesting due to the ferromagnetic nature of bulk Co: how is the magnetism affected by the chemical intercalation of Co into the cellulose matrix? If the magnetic properties are enhanced or diminished, is it related to nanostructure of individual particles, interparticle interactions or possibly even particle-matrix interactions? Wood is a natural nanostructured material, in which nanocrystallites of cellulose and several other biopolymers form a complicated microstructure. The structural properties of cellulose can be related to the macroscopic mechanical properties of wood. It turns out that x-ray diffraction is one of the most robust methods for the characterization of the microstructural properties of cellulose in wood.

Computational approaches to the calculation of average coordination numbers in nanocrystals in general are discussed in paper **III**. This can be regarded as a side note to the EXAFS analysis in paper **II**.

The last two papers (**IV** and **V**) discuss computational methods for the calculation of nanoparticle size-distributions in the framework of classical nucleation theory. Paper **IV** is a comparison between two different computational schemes. The first method is based on a kinetic Monte Carlo algorithm called the Particle Coalescence Method (PCM), and will not be discussed in this introductory part. The second method, which

is the Master Equation Discretization scheme (MED), is based on the direct numerical integration of the equations governing the cluster growth. In paper **V**, MED is applied to the growth of metallic clusters on wedged surfaces. In many respects, these are the first steps in modelling the nucleation and growth of metallic nanoclusters inside biopolymer matrices e.g. microcrystalline cellulose of paper **II**.

3 Materials

3.1 Cobalt nanoparticles

Magnetic nanoparticles have many applications and even more suggested potential applications, some of which are feasible in the near future and others are science fiction. Today they are used e.g. in ferrofluids, magnetic recording and giant magnetoresistance devices. Perhaps in the future they will used in biomedical applications such as precision drug delivery and cancer treatment by magnetic hyperthermia. [2] [14, Chs. 1&10]

Of all the elements abundant in Earth, only three are known that are ferromagnetic at room temperature (Fe, Co and Ni) [3, Ch. 3.2]. Nanoparticles composed of only one of these elements are called metallic nanoparticles. Metallic cobalt nanoparticles adopt at least three different crystal phases: face-centered cubic (FCC), hexagonal close packed (HCP) and epsilon (ϵ) [19]. The unit cells of these crystals are shown in Fig. 1. The crystal structure which emerges when Co-nanoparticles are manufactured depends on the preparation method and in some cases the particle size [20, 21]. For example, ϵ-cobalt is most often found in nanoparticles prepared by wet chemistry but is never found in bulk [3, ch. 3.2]. Bulk cobalt has HCP structure.

In addition to the aforementioned crystal structures, Co nanoparticles can adopt a quasicrystal-like structure known as the multi-twinned face-centered cubic (mt-FCC) lattice [3, Ch. 3], a.k.a. icosahedral particles [22, 23]. The multi-twinned particles are composed of domains with a distorted FCC lattice. Icosahedral particles can be assembled by bringing together twenty tetrahedral units at a common apex in the center of the particle. Although this structure has a 5-fold symmetry and no translational symmetry, i.e. the structure is by definition not a crystal, the diffraction pattern arising from the structure resembles the pattern of FCC-Co. Thus it is sometimes ambiguous whether the observed diffraction pattern relates to FCC or to mt-FCC [24].

In general, metallic magnetic nanoparticles are not stable in air, and are easily oxidized. This results in the change or loss of their magnetization. However, in some cases surface oxidation can have beneficial effects as well: enhanced magnetic properties have been observed for Co@Co-O[1] core-shell particles. This effect is explained by strong exchange coupling between the ferromagnetic Co core and the antiferromagnetic CoO layer. [3, Ch 3.2] [14, Ch. 1]

The stability of metallic nanoparticles can be enhanced by coating them with various surfactants, or manufacturing them inside inert polymer matrices [14, Ch. 3], such as polyethylene [14, Ch. 4] or cellulose [25, 26] (see also paper **II**). In addition to metallic cobalt and Co oxide nanoparticles, some preparation methods yield composite particles containing several elements (e.g. Co-B or Co-P), or magnetic alloys

[1] The notation refers to particles with a Co core and Co oxide shell.

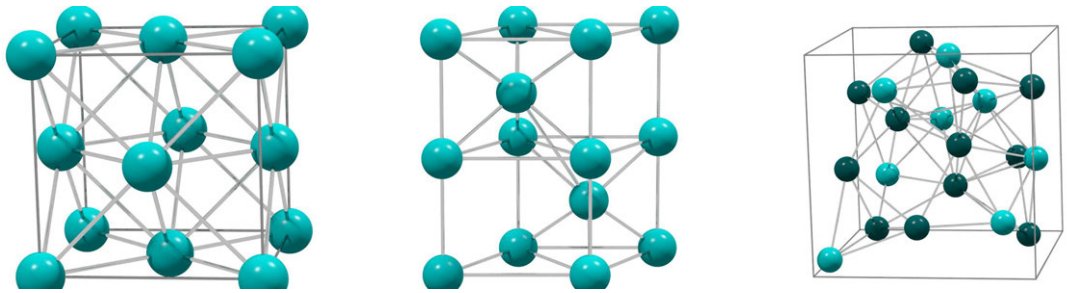

(a) FCC-Co (b) HCP-Co (c) ϵ-Co

Figure 1: Possible crystal structures for elemental cobalt. Blue balls represent positions of the Co-atoms inside the unit cell. In the case of ϵ-Co, there are Co-atoms with two types of coordination in the unit cell and these are distinguished by light and dark blue.

containing e.g. Co and Fe. In paper **II**, cobalt nanoparticles were manufactured by wet chemistry inside a microcrystalline cellulose matrix. Depending on the chemicals used in the synthesis, well ordered metallic Co nanoparticles were obtained in one case, whereas disordered Co-B and Co oxide composite particles were obtained in another. A short introduction into the making of nanoparticles is given in the introduction of paper **II**.

3.2 Cellulose

Cellulose is a naturally occurring linear polymer, which is composed of repeating units of beta D-glucopyranose units [27, Ch. 3.2]. Cellulose is used mostly as a construction material (as in the form of intact wood), as textile fibers and in the manufacturing of paper [28].

In its natural form, cellulose molecules form aggregates known as microfibrils, where well ordered (crystalline) regions alternate with less ordered (amorphous) regions. Crystalline cellulose exists in several different allomorphs, from which the cellulose Iα and Iβ are naturally occurring. The Iα phase, which is dominant e.g. in bacterial cellulose and valonia cellulose, has a triclinic structure and contains only one cellulose chain per unit cell. The Iβ phase, which is dominant in wood cellulose, has a monoclinic structure with two cellulose chains per unit cell (Fig. 2). The Iα phase is considered to be metastable, and can be transformed to Iβ by annealing. Cellulose II is probably the most important man-made allomorph of cellulose. It is manufactured, for example, by mercerization process or by regeneration, from cellulose I. Cellulose II has a monoclinic unit cell similar to Iβ, but with slightly different lattice parameters and antiparallel cellulose chain orientation. The transformation from cellulose I to cellulose II is considered irreversible. [8, 28]

Cellulose III_1 and III_2 can be manufactured by treating cellulose I or II by liquid

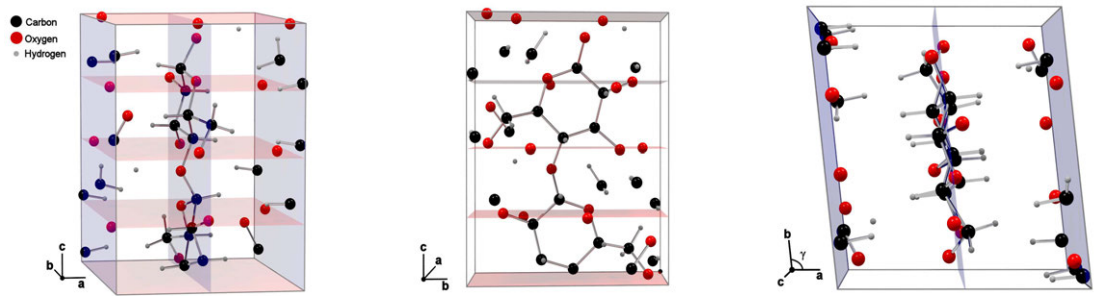

(a) (b) (c)

Figure 2: The monoclinic unit cell of cellulose Iβ from three perspectives. Using Miller indices (hkl), blue planes correspond to the 200-reflection and red planes to the 004-reflection.

ammonia. Both of these have the same monoclinic unit cell, but the packing of cellulose chains is different, with parallel arrangements in III_1 and anti-parallel ones in III_2. Furthermore, cellulose IV_1 and cellulose IV_2 are produced from the other allomorphs by heating in glycerol at 260°C. A triclinic unit cell is assumed for cellulose IV, but not much more is known due to poor quality of diffraction patterns obtained for this allomorph. It has been suggested that cellulose IV is very close to what can be considered less-ordered or amorphous cellulose. [8, 28] The nature of amorphous cellulose is discussed e.g. in a recent paper by Kontturi *et al.* [29]. However, the exact nature of what is actually meant by amorphous cellulose is currently still under debate.

Cellulose Iβ is the only allomorph relevant to this thesis, due to the fact that it is the dominant phase in microcrystalline cellullose of paper **II** and in Norway spruce of paper **I**. The unit cell of cellulose Iβ is shown in Fig. 2. The lattice constants of the monoclinic lattice (space group $P2_1$) are $a = 7.784$ Å, $b = 8.201$ Å, $c = 10.380$ Å and $\gamma = 96.5°$ [30, 31].

3.3 Norway spruce

Wood is a remarkable mesoscopic material with complicated structural features extending from nanoscopic to macroscopic size scales. The macroscopic structural and mechanical properties are linked to the underlying levels of the hierarchy, with each level contributing to the overall properties. The intricate details are a consequence of natural evolution and allow trees to withstand varying weather conditions, which in turn can be thought as the ultimate tensile tests on planet Earth. In order to make the most of wood as a construction material, or perhaps even mimic the properties of wood with modern composites, better understanding is required about the nano- and the microstructure of wood. [32–34]

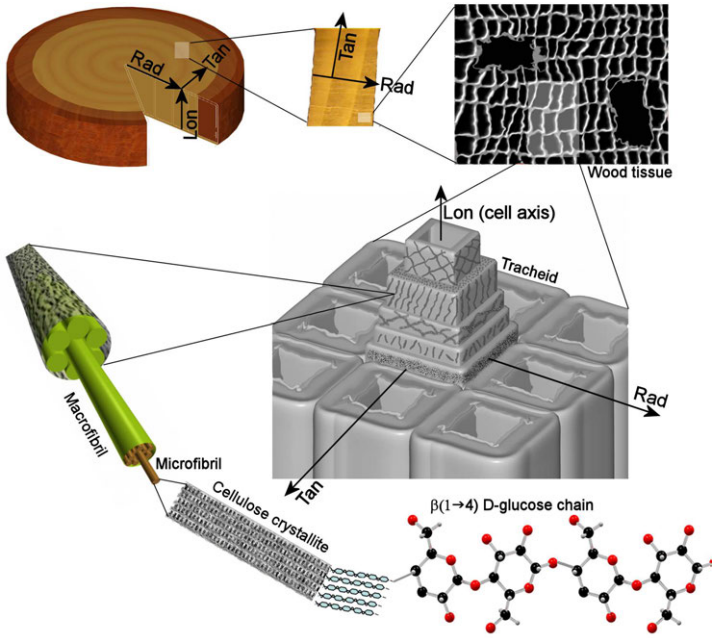

Figure 3: A simplified model of the hierarchical structure of wood from stem to atomic level, with the emphasis on structures relevant to this thesis. The arrows indicate the conventions used to describe directions in wood science. Rad is the radial direction, Lon is the longitudinal direction and Tan is the tangential direction. In the atomic size scale, black balls are carbon-, red balls are oxygen-, and grey balls are hydrogen atoms.

Norway spruce (*Picea Abies* [L.] Karst) is a coniferous tree native to Europe. Its structure can be divided into several length scales (Fig. 3). At the top of the size hierarchy is the entire stem with a girth as much as 4.7 meters (at breast height) and height up to 40 meters. The cross section of the stem consists mostly of a cellular structure known as the xylem (i.e. wood tissue), which is produced by a thin layer of living cells (cambium) between the xylem and the bark . The xylem can be divided into two visually and structurally distinct regions, earlywood and latewood. Earlywood is formed in the early stages of growth in spring and summer, and latewood is formed at the end of the growth season. The visual difference between these two regions gives the xylem the characteristic periodical ring-like structure along the radial path from the pith to the bark. Together, a one period of earlywood and latewood is referred to as an annual ring or growth ring. The properties of each ring can be related to the year the ring was formed. [35, 36] Figure 3 shows the conventions that have been used in paper **I** for coordinate axis directions when discussing the properties of wood. The longitudinal direction (Lon), also referred to as the longitudinal cell axis, is along the height of the tree. The radial direction (Rad) is from pith to bark and perpendicular to the growth rings. The tangential direction (Tan) is normal to the growth rings.

Most of the xylem consists of cells known as longitudinal tracheids. The longitudinal tracheids occupy up to 95% of the total volume of Norway spruce [32]. The rest of the volume is composed of ray parenchyma and ray tracheids. The tracheid is a needle shaped hollow tube with tapered ends, with a diameter between 25-45 μm and a length between 1-4 mm. The shape of the cross section varies from round to rectangular, and

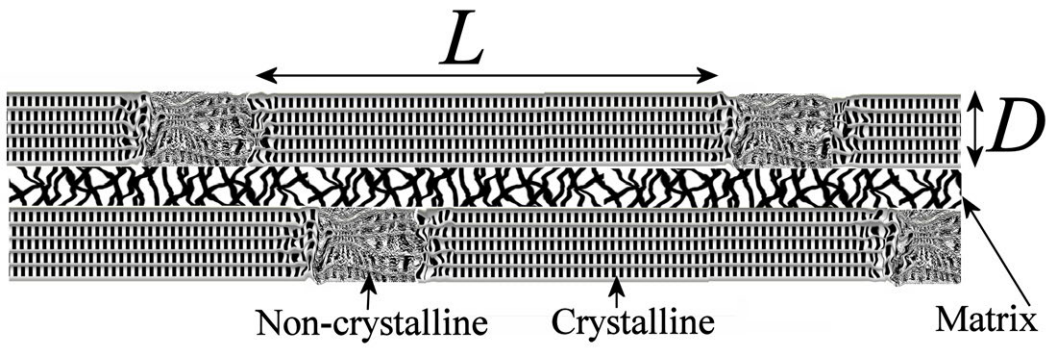

Figure 4: Simple model for cellulose microfibrils in wood. The length (L) and width (D) of cellulose crystallites can be determined by x-ray diffraction.

even hexagonal. [27, Ch. 1]

The cell wall of a tracheid is often divided into several layers according to the relative content of cellulose, lignin and hemicelluloses and the properties of cellulose fibrils. The two outermost layers are the middle lamella (ML) and the primary cell wall (P), after which comes the secondary cell wall (S). According to a generally accepted model (see e.g. [37] and references therein), the S-layer consists of three sublayers S1, S2 and S3, from which the S2 layer is the thickest (1-5 μm thick). The S2 layer has a particularly high content of cellulose, and the microfibril angle is generally smaller than in the neighboring layers. Due to the high thickness, high content of cellulose and relatively good orientation of cellulose microfibrils, the S2 layer is considered the most important single layer in the tracheid cell wall that contributes to the mechanical properties of wood. Due to similar reasoning, the x-ray diffraction pattern from xylem is nearly always explained by the structural properties of the S2 cell wall layer.

The cell walls are composites of cellulose fibrils and lignin/hemicelluloses matrix. A simple analogy is that the cellulose microfibrils have the same function as rigid steel rods have in reinforced concrete. Thus hemicelluloses and lignin act as the cement and sand filler. [35]

The basic building block of cellulose fibrils is the cellulose crystallite (Fig. 4). The microfibrils are considered to consist of alternating regions of well ordered cellulose (crystalline) and less ordered cellulose (amorphous). The average diameter D and length L of cellulose crystallites in Norway spruce are about 3 nm and 30 nm, respectively [38, 39]. The orientation of cellulose microfibrils with respect to the longitudinal cell axis is the microfibril angle (MFA).

4 X-ray synchrotron radiation in the study of materials

4.1 X-ray diffraction

The treatment of x-ray diffraction in this thesis is done in the framework of kinematic approximation. The main assumption is that the diffraction pattern is formed by photons which have scattered only once. The approximation is sensible in cases where the probability that a photon is scattered is low. The materials studied in this thesis are assumed to be weakly scattering. [18, Ch. 4] In contrast, the theory which does take into account the possibility of multiple scattering is dynamical diffraction. The contribution of multiply scattered photons is important in cases such as very well ordered crystals and single crystals. [18, Ch. 5] Dynamical diffraction will not be discussed further in this thesis.

X-ray diffraction is essentially an indirect probe since the diffraction pattern does not contain direct information about the spatial (or real-space) arrangement of building blocks from which the probed material is formed of. However, the diffraction pattern is related to the Fourier transform [40, Chs. 14-15] of the real space electron density. This abstract concept is referred to as the reciprocal space. Thus, in cases where real space electron density of the studied material is simple enough, or can be approximated as simple, it is possible to calculate the reciprocal space, and thereafter via comparison with the diffraction pattern, obtain direct information of the studied structure.

The second approximation used in this thesis is the utilization of the concept of crystal lattice [4, Ch. 2.2]. This essentially limits the volume where the electon density is non-zero to well defined positions with translational and rotational symmetry. This is indeed a model case of simplifying in order to understand the reciprocal space. It turns out that the reciprocal space of the crystal lattice also has a high degree of symmetry. This special case is referred to as the reciprocal lattice [4, Ch. 2.4] which has the following relationship with the real space lattice:

$$\mathbf{a_1^*} = 2\pi\frac{\mathbf{a_2}\times\mathbf{a_3}}{\mathbf{a_1}\cdot(\mathbf{a_2}\times\mathbf{a_3})};\ \mathbf{a_2^*} = 2\pi\frac{\mathbf{a_3}\times\mathbf{a_1}}{\mathbf{a_1}\cdot(\mathbf{a_2}\times\mathbf{a_3})};\quad \mathbf{a_3^*} = 2\pi\frac{\mathbf{a_1}\times\mathbf{a_2}}{\mathbf{a_1}\cdot(\mathbf{a_2}\times\mathbf{a_3})}, \tag{1}$$

where $(\mathbf{a_1}, \mathbf{a_2}, \mathbf{a_3})$ is the basis of the real space lattice and $(\mathbf{a_1^*}, \mathbf{a_2^*}, \mathbf{a_3^*})$ is the basis of the reciprocal lattice. [4, Ch. 3] [17, Ch. 4] [18, Ch. 4]

In a diffraction experiment, the directions of incident and scattered photons can be described with unit vectors $\mathbf{Q_0}$ and $\mathbf{Q}$. According to the Laue condition, diffraction is possible when the scattering vector $\mathbf{q} = (2\pi/\lambda)(\mathbf{Q} - \mathbf{Q_0})$ is equal to a vector $\mathbf{G}_{hkl} = (h\mathbf{a_1^*} + k\mathbf{a_2^*} + l\mathbf{a_3^*})$ that defines one of the reciprocal lattice points (h and k and l are integers known as Miller indices). The scattering geometry is illustrated as an Ewald construct [17, Ch. 1] in Fig. 5a, with the assumptions that the incident radiation is monochromatic and the reciprocal lattice is constructed from a FCC real space lattice.

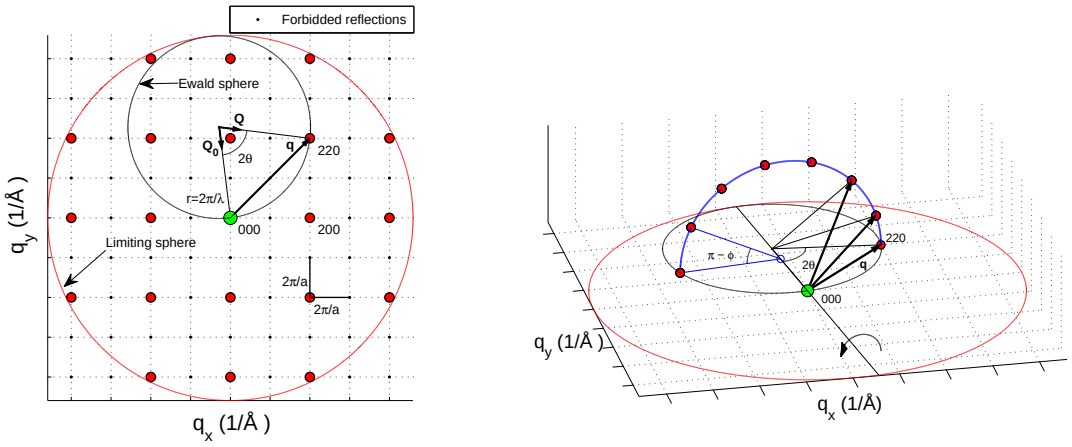

(a) (b)

Figure 5: In a) is an Ewald sphere construction in the $(q_x, q_y, 0)$-plane using a simple cubic basis and allowed reflections for FCC. Reciprocal lattice points marked with black dots are either forbidden reflections or are outside the limiting sphere, and are therefore not observed in diffraction. In b) the crystal is rotated in such way that the reciprocal lattice point 220 remains on the surface of the Ewald sphere.

With the aforementioned approximations and idealizations, the x-ray diffraction experiment is all about probing the positions, shapes and intensities of the reciprocal lattice points. For example, the positions of the reciprocal lattice points can be related to the distances of planes in the real space lattice. The shapes can be roughly related to the size of real space crystallites, and the intensities to the position and type of atoms inside the basic repeating unit, e.g. unit cell, of the real space crystal.

In some cases it is assumed that the crystals are randomly oriented with respect to the incoming x-ray beam. This is illustrated in Fig. 5b, where the crystal is allowed to rotate in such way that the respective reciprocal lattice point remains on the surface of the Ewald sphere and the geometry of the triangle defined by the Ewald sphere center and reciprocal lattice points 000 and 220 persist. A discrete rotation along the blue curve in Fig. 5b leads to a number of separate diffraction maxima (red dots) with the same scattering angle 2θ, differing only in the value of the azimuthal angle ϕ. Now if there are many crystals and their orientations are totally random, there are always crystallites in such orientations that each point of the blue curve will coincide with the respective reciprocal lattice point (red dot). This special case is referred to as powder diffraction. The circular diffraction pattern, which is observed in powder diffraction, is called the Debye ring of the respective reflection. Naturally, there are also cases where there is a partial orientation of crystals, i.e. the crystals are oriented in some direction with higher probability than in some other direction. In such cases it is possible to obtain information about the orientational distribution of crystals from the diffraction

pattern. For example, in this thesis, powder diffraction is utilized in the structural studies of microcrystalline cellulose and cobalt containing nanoparticles, whereas the diffraction from partially oriented crystals is utilized in the study of cellulose crystallites in wood.

4.2 Calculation of diffraction patterns

In the case of polycrystalline materials of known crystal structure, the diffraction pattern can be calculated analytically. The calculation can be divided into two parts: 1) finding the positions of the diffraction maxima (reflections) and 2) calculating the intensities for each reflection.

The positions of all the reflections for a given lattice can be calculated if the reciprocal lattice vectors (Eqs. (1)) are known. The elementary equation in diffraction, the Bragg's law [4, Ch. 3] states that

$$2d_{hkl} \sin \theta_{hkl} = \lambda, \tag{2}$$

where d_{hkl} is the distance between the planes hkl in the real-space lattice. According to the geometry of Ewald construction (e.g. Fig. 5a), the magnitude of the scattering vector, which coincides with the reciprocal lattice point hkl, is

$$|\mathbf{q}_{hkl}| = \frac{4\pi \sin \theta_{hkl}}{\lambda}, \tag{3}$$

where λ is the wavelength of incident radiation and θ is the Bragg angle. When Eqs. (2) and (3) are combined, a useful relation is obtained:

$$|\mathbf{q}_{hkl}| = |\mathbf{G}_{hkl}| = |(h\mathbf{a}_\mathbf{1}^* + k\mathbf{a}_\mathbf{2}^* + l\mathbf{a}_\mathbf{3}^*)| = \frac{2\pi}{d_{hkl}}, \tag{4}$$

i.e. the magnitude of the scattering vector which satisfies the Laue condition has a trivial reciprocal relationship with the distance between the planes (hkl). Eq. (4) allows the calculation of analytic formulae for d-values in all the Bravais lattices, and combined with Eqs. (2) and (3) it gives the positions of the diffraction maxima as a function of θ (°) or q (1/Å). The q-scale is often preferable because it is invariant of the wavelength of incident radiation.

The intensity of each reflection hkl depends on the positions of the atoms inside the unit cell. The unit cell form factor (i.e. scattering amplitude) for the reflection hkl is [4, Ch. 3]

$$F_{hkl} = \sum_n f_n \exp(2\pi i(hx_n + ky_n + lz_n)), \tag{5}$$

where f_n is the scattering factor and (x_n,y_n,z_n) are the coordinates of the n^{th} atom. The sum runs over all the atoms that belong in the unit cell. The general form of the atomic scattering factor is [17, Ch. 1] [41, Ch. 4.2.6]

$$f(q, E) = f^0(q) + f'(q, E) + if''(q, E), \tag{6}$$

where total atomic scattering factor $f(q, E)$ is divided into three parts for convenience. The term $f^0(q)$ is the atomic form factor, which is basically the reciprocal space representation of the electron density around the nucleus of the atom. The terms $f'(q, E)$ and $f''(q, E)$ are correction factors that are significant when the energy of incident radiation is near an absorption edge of the respective atom. The *ab initio* calculation of these terms requires complicated quantum mechanical electron structure calculations. Fortunately, values for these terms have been tabulated for most atomic elements and ions [41, Ch. 4.2.6] (see also `http://skuld.bmsc.washington.edu/scatter/AS_form.html` and `http://www.nist.gov/pml/data/ffast/index.cfm`).

In most cases, including the diffraction studies of this thesis, the total scattering factor can be conveniently approximated as $f(q, E) \approx f^0(q)$. The correction factors are essential only in few specialized diffraction techniques such as anomalous wide angle x-ray scattering (AWAXS) and anomalous small-angle x-ray scattering (ASAXS) [42,43]. Probably the most effortless way to obtain values for $f^0(q)$ is the so-called analytic approximation [18, Ch. 4]

$$f^0(\frac{\sin\theta}{\lambda}) = \sum_{j=1}^{4} a_j \exp\left(-b_j \frac{\sin^2\theta}{\lambda^2}\right) + c, \tag{7}$$

where a_j, b_j and c are tabulated constants [41, Ch. 6.1] .

For a polycrystalline material, the diffraction intensity for each reflection hkl is [4, Ch. 4]

$$I(q) = I_0 p G(q) |F_{hkl}|^2, \tag{8}$$

where I_0 is the intensity of the incident radiation and p is the multiplicity factor (i.e the number of planes with same interplanar distance d_{hkl} in the unit cell). The term $G(q)$ incorporates all the necessary factors arising from the experimental setup and the sample geometry.

In the special case of an ideal crystallite of infinite size and perfect experiment resolution, the reflection is a delta peak $I(q)\delta(q - q_{hkl})$. Practically this it not the case and the reflections are broadened by 1) the limited resolution of experiment and 2) the breakup from the model of an ideal crystal. The shape of the broadened reflection is often similar to Gaussian or Lorentzian distributions, and in some more complicated cases a linear combination or convolution of these (i.e. pseudo-Voight or Voight distributions). It should be noted that the intensity given by Eq. (8) is the *integrated intensity*, i.e. the area under the distribution which constitutes the reflection.

Similar method of calculating diffraction patterns is implemented e.g. in the computer programs PowderCell [44] and Mercury [45], which provide a relatively simple graphical interface to visualize crystal structures, and to calculate and evaluate their powder diffraction patterns. The limitation of the method is that it does not reproduce either the effects of crystallite size and shape in the patterns or the smooth features of small-angle scattering curves or scattering from less-ordered materials.

In order to model the diffraction patterns of very small crystallites (nanocrystals) and less-ordered particles of arbitrary shape, a different method is required. If the atomic coordinates of the particle are known, the orientationally averaged intensity can in principle be calculated with the Debye function [17, Ch. 2.6]

$$\langle I(q)\rangle = \sum_m \sum_n f_m^* f_n \frac{\sin(qR_{mn})}{qR_{mn}}, \tag{9}$$

where R_{mn} is the distance between atoms m and n, and the sums run over all the atoms in the particle. This form of the Debye function is not very convenient for modelling due to the fact that the double sum over all the atoms results in N^2 scaling in calculation times (N is the number of atoms). By calculating explicitly the cases $m = n$, and including the cross terms ($m \neq n$) only once, the Debye function reduces to

$$\langle I(q)\rangle = N|f|^2 + 2\sum_{m>n} f_m^* f_n \frac{\sin(qR_{mn})}{qR_{mn}}, \tag{10}$$

which is equivalent to Eq. (9) and computationally slightly more efficient. Even so, this method is still limited to smaller systems since the time needed for the calculations scales as $N(N-1)/2$, which is $\sim N^2$ for large N.

4.3 Diffraction from cellulose microfibrils

X-ray scattering methods are well suited in the study of nanostructural arrangement of cellulose in wood. For example, in x-ray diffraction (XRD or WAXS) the diffraction pattern arising from the crystallites of cellulose allows the determination of average dimensions of cellulose crystallites and the microfibril angle distribution [38, 39, 46]. Small-angle x-ray scattering (SAXS) can be used to determine the shape, size and orientation of the cellulose nano- or microfibrils. The advantage of XRD over SAXS arises from the signal-to-noise ratio: the interesting and worthwhile information comes from the intensive diffraction peaks which often dominate over the scattering arising from other components of the system e.g. non-crystalline cellulose, lignin or hemicellulose. The determination of the microfibril orientation using SAXS is quite straightforward and can be used reliably on pristine wood samples [32, 47].

In paper **I** the nanostructure of cellulose microfibrils in Norway spruce is studied by x-ray diffraction. The experimental setup is shown in Fig. 6 and discussed further in paper **I**.

The cellulose microfibril axis is oriented in the plane of the cell wall with respect to the cell axis (Fig. 7a), and the orientation angle is referred to as the microfibril angle (MFA). The cross sectional profile of the fibril is randomly oriented. The incident x-ray beam is normal to the front cell wall. In the following the diffraction pattern of such system is discussed.

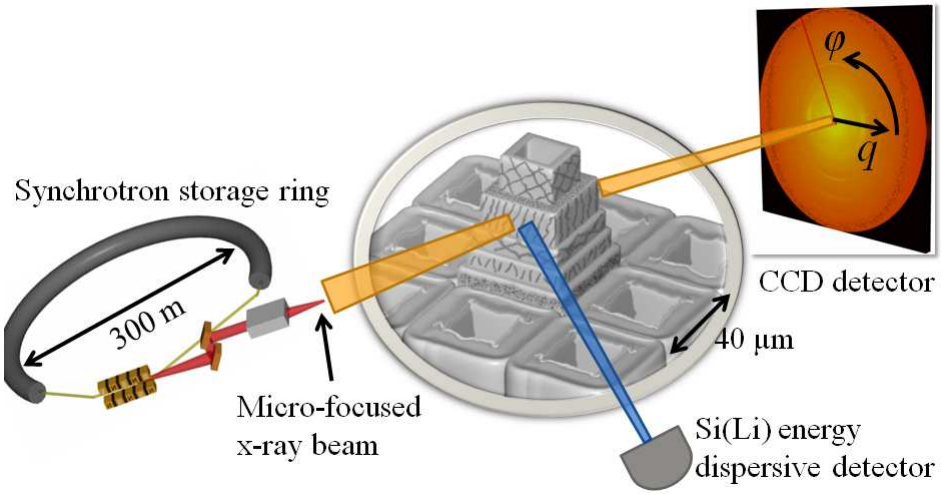

Figure 6: A scheme showing the x-ray microanalysis setup at the beamline ID18F, ESRF. X-ray diffraction and x-ray fluorescence were simultaneously measured from sections of wood containing wood cells (tracheids).

In this case the fibril consists of cellulose Iβ crystallites (Fig. 2). The lattice vector **c** is the oriented fiber axis, and **a** and **b** are the non-oriented axes. The strongest reflections are the randomly oriented 110, $1\overline{1}0$, 200 and the oriented 004. The determination of crystallite size and orientation is done using the 200 reflection due to the fact that it is theoretically the strongest reflection and the overlaps with other significant reflections are minimal.

The reciprocal space representation of an oriented cellulose crystal, within a cell wall with a rectangular cross section, is illustrated in Figs. 7b and 7c. In the former figure the MFA is zero and only one reciprocal space "ring" per reflection is observed. According to the intersection between the ring and the Ewald sphere, two equatorial spots for reflection 200 are seen in diffraction. In the latter figure the MFA is non-zero (15°), and the reciprocal space rings from all the four cell facets are resolved. The intersections with the Ewald sphere indicate that now 8 spots (for the 200 reflection) are seen in diffraction. When the diffraction patterns are recorded on a flat 2-dimensional detector (e.g. Fig. 6), all the eight spots for the 200 reflection have the same magnitude of scattering vector q, and therefore the same scattering angle 2θ, but are seen at different azimuthal angles φ in the plane of the detector. The relationship between the MFA (μ) and φ is known as the Cave's equation [48]

$$\tan\theta\cos\alpha + \sin\alpha\cos\varphi + \cot\mu\sin\varphi = 0. \tag{11}$$

This equation also takes into account the possibility that the cell wall is rotated around the cell axis with respect to the incoming beam via the parameter α, which is defined as $(90° - rot)$, where rot is the counterclockwise rotation of the front cell wall in relation

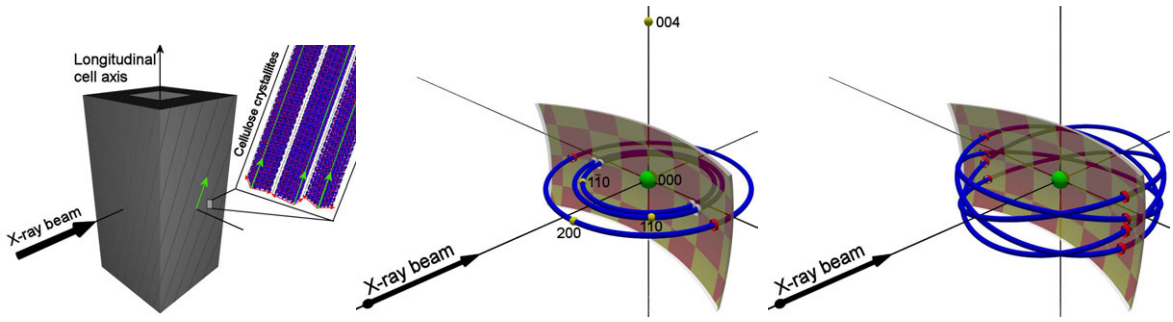

(a) Real space. (b) Reciprocal space. MFA=0°. (c) Reciprocal space. MFA=15°.

Figure 7: A simple model for the cellulose microfibril angle determination. In a) the x-ray beam is incident at right angles with respect to the front cell wall. The cell wall is composed of oriented cellulose crystals. In b) the reciprocal space representation of reflections 110, $1\overline{1}0$, 200 and 004 are shown. In c) only reflection 200 is shown.

to the incident x-ray beam. An analytic solution is found by transforming Eq. (11) into a quadratic equation [49]

$$\begin{aligned} &a\cos^2(\varphi) + b\cos(\varphi) + c = 0, \text{ where} \\ &a = \sin^2(\alpha) + \cot^2(\mu), \\ &b = \tan(\theta)\sin(2\alpha), \text{ and} \\ &c = \tan^2(\theta)\cos^2(\theta) - \cot^2(\mu), \end{aligned} \tag{12}$$

and solving for $\cos(\varphi)$. Using this model the MFA is determined from the diffraction pattern with numerical least-squares fitting. The details of the fitting procedure are discussed in the Sec. 2 of paper **I**.

4.4 Extended x-ray absorption fine structure spectroscopy

In x-ray absorption spectroscopy (XAS) the attenuation of electromagnetic radiation is studied as a function of energy of the radiation. The attenuation of radiation inside material is given by Beer's law

$$I = I_0 \exp(-\mu x), \tag{13}$$

where I_0 is the intensity of the incident beam, I is the intensity of the transmitted beam and x is the thickness of the material and μ is the linear absorption coefficient. By varying the energy E of the incident radiation, the dependence of the absorption coefficient as a function of energy can be determined as

$$\mu(E)x = -\log\frac{I}{I_0}. \tag{14}$$

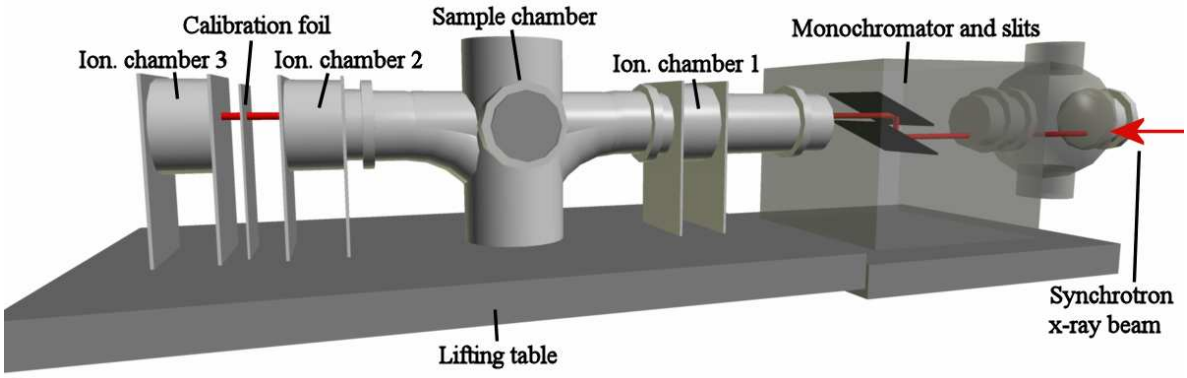

Figure 8: A scheme showing the experimental setup for x-ray absorption spectroscopy at the beamline X1 in DESY.

In the x-ray energy region it turns out that μ approximately depends on the fourth power of the atomic number and the reciprocal of third power of energy [50, Ch. 1]. Near a certain element specific threshold energies, the absorption coefficient suddenly increases as a function of energy. These regions in the absorption spectrum are the absorption edges (left side of Fig. 9). The absorption edge is detected when the energy of incident radiation crosses a threshold E_0, which is very near the energy required to excite an electron from one of the atomic orbitals or suborbitals to the continuum (i.e. photoionization). The so-called photoelectron can be consided as an outgoing spherical wave with a wavevector of magnitude [50, Ch. 2]

$$k = \sqrt{\frac{2m_e}{\hbar^2}(E - E_0)}. \tag{15}$$

The photoelecton may be scattered from neighboring atoms any number of times and the final state is a superposition of the outgoing and scattered waves. This interference modulates the probability of photoelectric absorption, which in turn is detected as oscillations in the absorption spectrum right after the absorption edges (right side of Fig. 9).

In practice, the oscillatory part is separated into two parts: the x-ray absorption near edge structure (XANES) and the extended x-ray absorption fine structure (EXAFS) [51, Ch. 2.4]. The former includes the region with photoelecton energies $(E-E_0)$ from 0 eV to about 40 eV and the latter from 40 eV to about 1000 eV. The XANES region is dominated by multiple scattering events, and yields information about the symmetries and chemical state in the immediate neighborhood of the absorbing atom. The EXAFS region is dominated by single scattering events, and yields information about the coordination of atoms near the absorbing atom.

In the single (back)scattering picture, the interference between the ongoing and once backscattered photoelectron waves can be expressed mathematically as $a(k)\sin[2kr +$

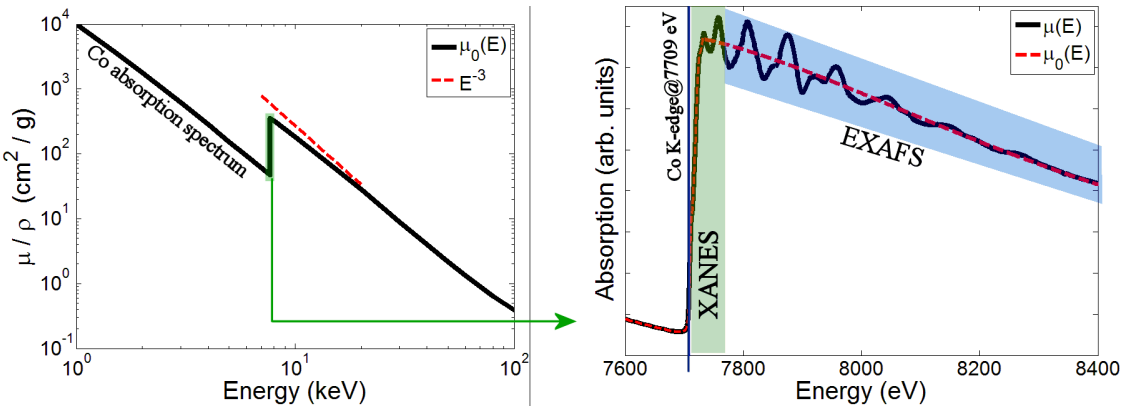

Figure 9: A schematic representation showing the absorption spectra of cobalt at x-ray energies. The figure on the left shows the general features of the spectrum (NIST database at `http://www.nist.gov/pml/data/xraycoef/index.cfm`) and the figure on the right shows the fine structure at the K-absorption edge for bulk cobalt and the division of the spectra to XANES and EXAFS regions.

$\phi(k)]$, where r is the distance between absorbing and scattering atoms, $a(k)$ is an amplitude term including modulation and damping effects, and $\phi(k)$ is total phase shift including the effects of both absorber and backscatterer [51, Ch. 2.4].

In the case the neighboring atoms are quite well localized in concentric "coordination shells" around the absorbing atom (as in crystalline solids), the oscillations can be modelled with the EXAFS equation, which is basically a superposition of interferences from all the shells j

$$\chi(k) = S_0^2 \sum_j \frac{N_j |f_j(k)|}{k r_j^2} \exp(-2\sigma_j^2 k^2 - \frac{2r_j}{\Lambda(k)}) \sin(2kr_j + 2\delta_c(k) + \phi_j(k)), \qquad (16)$$

where $|f_j(k)|$ is the magnitude of backscattering amplitude from each of the N_j neighboring atoms r_j distance away. The phase shifts experienced by the photoelectron are taken into account by terms $\delta_c(k)$, which is the shift due to absorber and $\phi_j(k)$, which is the shift due to backscatterer. The overall scaling of amplitudes due to the absorbing atom is taken into account by the term S_0, which is here assumed independent of k. The dissipation of EXAFS signal as a function of k is governed by the exponential decay due to static and thermal disorder in the material (Debye-Waller factor σ) and the photoelectron mean-free path $\Lambda(k)$. In practice the oscillations are adequately detected only to $k = 20$ Å^{-1}. The spatial distance of detectable shells is limited e.g. by the $1/r^2$ dependence and k-resolution of the experiment, which makes EXAFS sensitive only up to four nearest coordination shells. [52, 53]

Aside from the single scattering approximation, the full theoretical determination of the oscillations requires electronic structure calculations for the absorbing atom and all atoms within a certain cut-off radius, and the modelling of all the possible scattering

paths of the photoelectron. This method is referred to as the full multiple scattering (FMS) formalism [54]. The multiple scattering formalism is required for quantitative description of XANES, and it is outside the scope of this thesis.

In paper **II**, cobalt-containing nanoparticles in cellulose matrix were characterized with x-ray absorption spectroscopy at the Co K-absorption edge at the beamline X1 in DESY, Hamburg (Fig. 8). The XANES region was only used for "fingerprinting", i.e. the XANES spectra were compared with known spectra of metallic Co and Co oxides. Fingerprinting allows for a qualitative determination of the average oxidation state of the absorbing atom species without the need for rigorous FMS calculations. The EXAFS region was used for quantitative determination of the chemical neighborhood around Co atoms by fitting Eq. (16) to the measured oscillations. The details of the data analysis are given in Sec. 3.4 of paper **II**.

4.5 X-ray fluorescence spectroscopy

The emission of characteristic x-rays from core electron shells of atoms can be used as fingerprints to identify the elements. In x-ray fluorescence spectroscopy (XRF), an electron bound to one of the core electronic shells, with energy E_1 is excited by x-ray radiation, creating a core-hole in the respective shell. The hole is subsequently filled by an electron from a higher energy shell E_2. The relaxation leads to the emission of a quantum of electromagnetic radiation with an energy of $h\nu = \Delta E = E_2 - E_1$. Each possible transition between two energy levels has its own energy difference ΔE, and these differences are dependent on the electron shell structure i.e. the type of atom [50, Ch. 1.4]. Thus, by measuring the energies of these characteristic lines and comparing them to known values for various elements, the element composition of the studied material can be determined. In addition, the integrated intensities of the characteristic lines can be used for quantitative analysis i.e. the determination of element concentrations.

In quantitative XRF, the raw detector counts within characteristic lines of element Z must be normalized to take into account all the effects arising from the sample and the experimental geometry. One possibility is the fundamental parameter approach, where most of the necessary equations and parameters contributing to the total fluorescence yields are assumed known, and the unknown parameters (e.g. element concentrations) are determined by fitting the model to the measured data [55]. The second option is to use the fluorescence spectrum from a sample with known element composition as a reference, thereby eliminating most of the fundamental parameters in the equations relating the intensity of the fluorescence line I and the concentration of the element Z [56].

In paper **I**, The XRF spectra were used for the determination of nutrient element concentrations in wood. All the spectra included characteristic peaks from elements

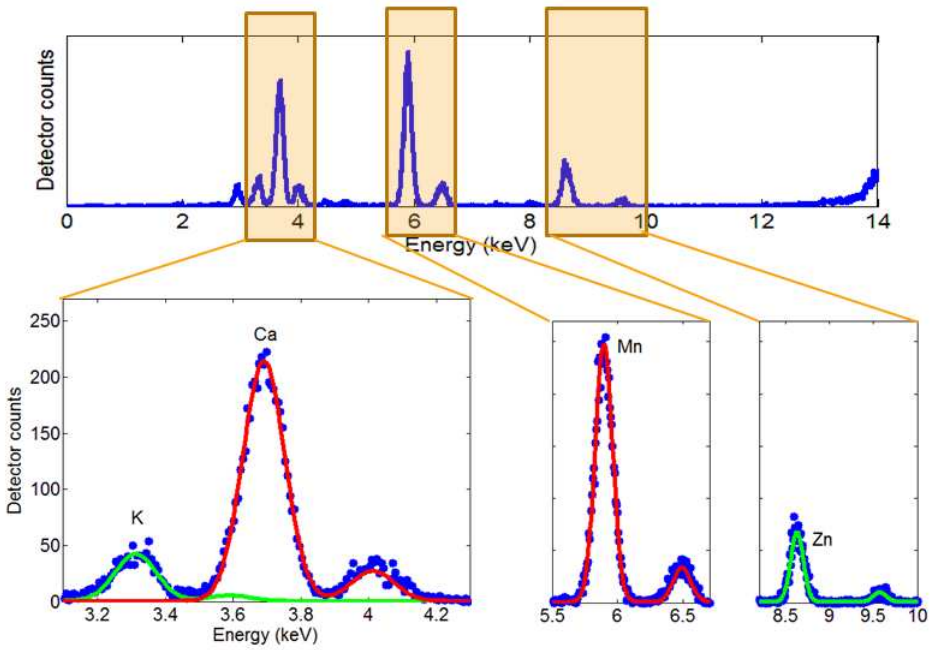

Figure 10: Fluorescence spectrum of wood. The fluorescence peaks from K, Ca, Mn, and Zn are highlighted. Blue dots are measured detector counts and green and red are fitted models.

Cl, Ar, K, Ca, Ti, Mn, Cu, and Zn. Trace amounts of elements of lower atomic number than Ar ($Z = 18$) could not be detected accurately with the particular experiment.

The data analysis was mostly done with the PyMca (Python Multichannel analyzer) 4.3.0 fluorescence analysis software [57]. The raw fluorescence spectra were fitted with a model using theoretical K-fluorescence lines of Cl, Ar, K, Ca, Ti, Mn, Cu, and Zn. The fitted model did not include fluorescence generation from higher shells (e.g. L- or M-shells), scattering peaks and escape peaks. Figure 6 shows a scheme of the experiment and Figure 10 shows an example of one of the fluorescence spectra measured from Norway spruce. The details of the quantitative fluorescence analysis are given in Sec. 2.2 of paper **I**.

5 Computational methods for modelling nanocluster growth

An interesting problem in the growth of nanoclusters is size selection i.e. the existence of optimal or preferred cluster sizes. Spontaneous size selection is known to occur e.g. in two and three dimensional heteroepitaxial growth of semiconductor and metallic clusters [58, 59]. The physical origin of size selection is attributed to the existence of a minimum in the cluster formation energy [60]. However, energetics alone is insufficient to describe some of the properties of size selection, for example the formation of metastable stationary states outside the energy minimum [61]. Rather it seems that a satisfactory model should also include kinetic considerations, and therefore also the interplay between energetics and kinetics of growth. The consequent complexity of the growth problem requires a computational approach, and the traditional methods include Molecular Dynamics (MD) and Kinetic Monte Carlo (KMC) simulations. However, in many cases of interest, time scales and ensemble sizes required are at the moment beyond the capabilities of MD. Kinetic Monte Carlo methods have been used succesfully to reproduce the size selection, but the obtained size distributions are statistically inaccurate. Therefore it is sensible to model size selection at the mesoscopic scale.

The mesoscopic size scale refers to such length scales, where one can reasonably discuss the properties of a material or phenomena without having to discuss the behavior of individual atoms. For solids and liquids this is typically from a few to ten nanometers, and involves averaging over a few thousand atoms or molecules. Thus the mesoscopic scale is roughly equivalent to the nanoscopic scale.

This section describes the Reaction Kinetic Model (RKM), which is the mesoscopic scale cluster growth model used in papers **IV** and **V**. The first part introduces the rate equations governing the growth. These equations are based on the standard kinetic equations in classical nucleation theory, also known as Becker-Döring equations [62]. After that the energetics and kinetics are discussed at some length.

5.1 Nucleation kinetics of isolated clusters

Let isolated nanoclusters be composed of s arbitrary building blocks or particles. These blocks can be e.g. atoms or molecules. The number density of clusters of size s is n_s, so that n_1 refers to monomers, n_2 to dimers, n_3 to trimers and so forth. Particles grow and shrink by addition or subtraction of one monomer. The clusters with $s > 1$ are isolated from each other so they cannot combine. Thus all the reactions are single step processes $s + 1 \rightleftharpoons (s + 1)$ (Fig. 11).

The forward reaction is certainly proportional to the number of monomers and clusters of size s, so the reaction rate can be written as $n_1 n_s \sigma_s$, where σ_s is the "affinity"

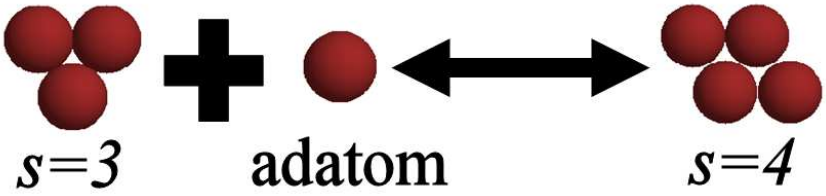

Figure 11: The creation a cluster of size 4 from a cluster of size 3 and an adatom. The reaction is assumed reversible.

for a cluster of size s to capture a monomer. Similarly the backward reaction rate can be written as $n_{s+1}\gamma_{s+1}$, where γ_s is the affinity for a cluster of size s to release a monomer. The parameters σ_s and γ_s are hereafter referred to as the attachment rate and detachment rate, respectively. The net rate of creation of $(s+1)$ clusters from s clusters is the flux [63, 64]

$$J_s = n_1 n_s \sigma_s - n_{s+1}\gamma_{s+1}. \tag{17}$$

Furthermore, the net rate of creation of s clusters is due to their creation from $s-1$ clusters minus the net rate of creation of $s+1$ clusters (Eq. (17))

$$\dot{n}_s = J_{s-1} - J_s = \sigma_{s-1} n_{s-1} n_1 - \sigma_s n_s n_1 + n_{s+1}\gamma_{s+1} - \gamma_s n_s, \text{ for } s \geq 2. \tag{18}$$

The time evolution of monomers (or adatoms) can be obtained by imposing a constraint to the total mass ($M = \sum s n_s$) of the system: the total mass must be constant in time, unless more adatoms are deposited i.e. $dM/dt = \phi$, where ϕ is the deposition flux of adatoms. The time evolution of the adatom density can now be written as a function of Eq. (18)

$$\dot{n}_1 = \phi - \sum_{s \geq 2} s\dot{n}_s \tag{19}$$

The final forms of these equations, referred to as the Reaction Kinetic Model, are discussed in the following.

5.2 The rate equations governing the growth

In paper **IV**, the cluster growth is described by the Reaction Kinetic Model (RKM) [61] based on Eqs. (18) and (19)

$$\frac{dn_1}{dt} = \phi - 2\sigma_1 n_1^2 - n_1 \sum_{s \geq 2} \sigma_s n_s + \kappa\gamma_2 n_2 + \sum_{s \geq 2} \kappa\gamma_s n_s \tag{20}$$

$$\frac{dn_s}{dt} = \sigma_{s-1} n_{s-1} n_1 - \sigma_s n_s n_1 + \kappa\gamma_{s+1} n_{s+1} - \kappa\gamma_s n_s, \tag{21}$$

where κ defines the ratio of the total detachment rate to the total attachment rate, and it essentially modifies the time scale of growth.

These rate equations are extremely difficult to solve for size distributions. In addition, the numerical solution methods are bottlenecked by the term governing the time evolution of adatom density. In paper **V**, an attempt is made to bypass this bottleneck by simplifying the rate equations. Eqs. (20) and (21) are first divided with κ and the term n_1/κ is defined as the scaled adatom density N_1. Furthermore, the scaled adatom density is assumed stationary in time ($dN_1/dt = 0$), and the direct merging of two adatoms to form dimers is prevented ($N_1\sigma_1 n_1 = 0$). This leads to an approximate form of the rate equations

$$\begin{aligned} \frac{dN_1}{dt} &= 0 \\ \frac{dn_2}{d\tau} &\simeq -(N_1\sigma_2 + \gamma_2)n_2 + \gamma_3 n_3 \qquad (22) \\ \frac{dn_s}{d\tau} &= \sigma_{s-1}n_{s-1}N_1 - \sigma_s n_s N_1 + \gamma_{s+1}n_{s+1} - \gamma_s n_s, \qquad (23) \end{aligned}$$

where $d\tau = \kappa dt$. The stationary state adatom density can now be calculated explicitly as

$$N_1^{stat} = \frac{\Phi + \gamma_2 n_2 + \sum_{s\geq 2}\gamma_s n_s}{\sum_{s\geq 2}\sigma_s n_s}, \qquad (24)$$

where $\Phi = \phi/\kappa$ is now the scaled deposition flux. This approximate form is not expected to produce the actual time evolution realistically; thus equations (20) and (21) should rather be used if one were to study in detail the intermediate stages before the stationarity is reached.

5.3 The energetics and kinetics of growth

The functional forms for the attachment rate σ_s and the detachment rate γ_s depend on the particular growth problem. As such, these terms contain all the "physics" in the RKM. Since attachment and detachment are assumed reversible, the growth must be slow enough to allow the system to reach equilibrium between the reactions. At equilibrium the flux J_s (Eq. (17)) is zero, which leads to the relation

$$\frac{\gamma_{s+1}}{\sigma_s} = \frac{n_1 n_s}{n_{s+1}}. \qquad (25)$$

As an analogy to statistical thermodynamics, at any stage of growth the system consists of clusters of size s, with respective free energies E_s (energy levels) and energy level populations n_s. In the time scale of one reaction, it is assumed that the total number of particles ($\sum n_s$) and the total energy ($\sum E_s n_s$) are constant. The statistical distribution that follows from these constraints is the Boltzmann Distribution Law [65, Ch. 2] [66, Ch. 23.2] i.e. in this case $n_s \sim \exp(-E_s/k_B T)$. Combined with Eq. (25), the *principle of detailed balance* [66, Ch. 12.4] [67] is obtained:

$$\frac{\gamma_{s+1}}{\sigma_s} \sim e^{\beta\Delta_s}, \qquad (26)$$

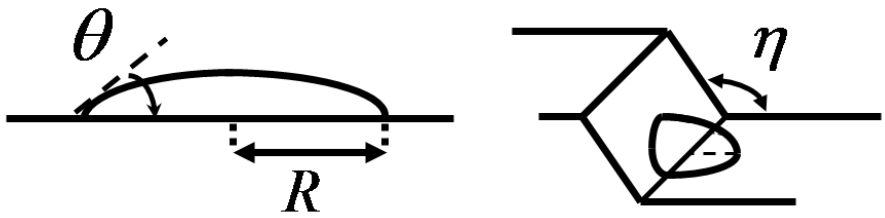

(a) (b)

Figure 12: The growth on (a) flat and (b) wedged surface. R is the radius of the cluster, θ is the cluster-substrate contact angle and η is the wedge opening angle.

where β is $(k_B T)^{-1}$ (k_B is the Boltzmann constant and T is the absolute temperature) and $\Delta_s = E_{s+1} - E_s$ is the free energy difference of clusters of size s and $s+1$. The energy difference Δ_s essentially describes the energy needed to remove or add one atom to the dot of size s, and in the continuum limit it relates to the chemical potential $\mu(s) = (\partial E/\partial s)$.

The attachment and detachment rates are defined according to the self-consistent rate theory of Bales and Zangwill [68] for reversible nucleation and growth of 2D islands. However, the functional form of these equations is simplified in order to reduce the amount of parameters in the model. The simplifications lead to mathematically simple forms of the rates [61]

$$\sigma_s = s^q/(1 + e^{\beta\Delta_s}) \quad (27)$$

$$\gamma_s = s^q/(1 + e^{-\beta\Delta_{s-1}}), \quad (28)$$

which are qualitatively similar to the original theory. The geometric size dependence of the reaction rates is taken into account by a simple power law s^q, where q is related to the morphology of the growing dots.

The models for energetics of growth in paper **IV** and paper **V** are described by parametrised power laws, which are not directly related to any particular system. This is mainly because this would require knowledge about specific parameters such as the surface energies of clusters and substrate, island-substrate interface energies and contact angles. Hence the energetics here can be thought as generic, valid for a large class of systems.

In paper **IV** the energetics are defined according to a phenomenological model proposed by Gai *et al.* for the self-assembly of metallic nanodots [59]. This leads to a generic form for the free energy difference of clusters

$$\Delta_s = c\, s^{\alpha} + a\, s^{-p} + w_0. \quad (29)$$

where the first term is related to the self-energy of an isolated cluster and the second term is related to the energy due to cluster-cluster interactions. Parameters a, c and

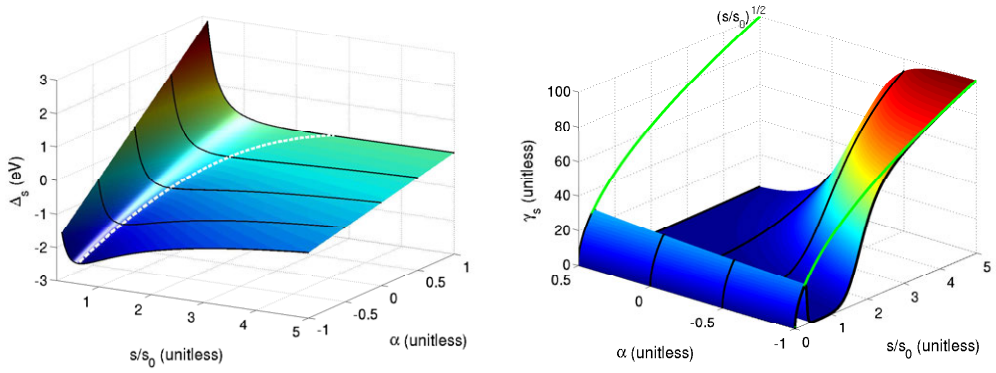

(a) (b)

Figure 13: The free energy difference (a) and the resulting detachment rates (b) in paper **V**. In Fig. (a) the white dashed line marks the free energy difference minimum as a function of the parameter α. In Fig. (b) the green line marks the attachment rate ($\sigma_s \approx s^{1/2}$).

w_0 are constants. The intricate details behind this parametrisation are not discussed further, and Eq. (29) is mainly treated as a convenient and flexible fitting formula for several possible types of energetics of different physical origin. In addition, the simple functional form of Eq. (29) is convenient for the benchmarking and comparison between the two simulation methods of paper **IV**.

In paper **V**, the energetics are defined according to a physically more realistic model of Liu [69], which explicitly takes into account contributions from the cluster surface energy and additional energies associated with cluster edges. In the case that the nucleating clusters are isolated spherical caps on top of a substrate (Fig. 12a), the free energy difference can be written as

$$\Delta_s(x) = -x^{-1}\log(ex) + 2\alpha e^{-\frac{1}{2}}x^{-\frac{1}{2}}, \tag{30}$$

where x is the scaled size of the cluster (s/s_0), and s_0 is the cluster size at the energy minimum. The first term corresponds to the cluster-substrate edge energy and the second term corresponds to the surface energy of the cluster. The cluster-cluster interaction is assumed negligible. The free energy difference surface and the resulting reaction rates defined by Eq. (30) are shown in Figs. 13a&b in the parameter space of paper **V**.

Although not really in the scope of this thesis, it must be added that the detailed description of the α-parameter is essential in relating the underlying model with real systems. For example, in Liu's model [69], the α-parameter is described as

$$\alpha = \frac{G(\eta,\theta)}{\sin^2\theta}\cdot 4R_0\frac{\epsilon_m}{\epsilon_d} \tag{31}$$

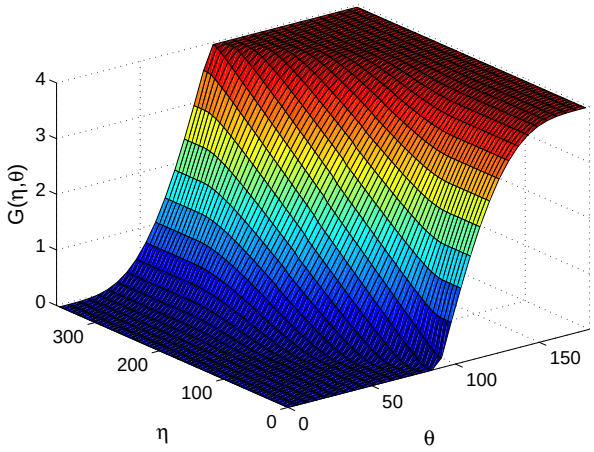

Figure 14: The relationship between the contact angle θ, the wedge opening angle η and the geometrical factor G according to Sholl and Fletcher [70].

where ϵ_m is the surface energy of the cluster, ϵ_d is the elastic energy per unit length of cluster edges and R_0 is the cluster radius at free energy minimum. The geometric factor $G(\eta, \theta)$ is known [70], and it can be related to the opening angle of the wedge (η) and to the cluster to substrate contact angle (θ): the possible values for $G(\eta, \theta)$ lie on the surface shown in Fig. 14.

However, the remaining terms in Eq. (31) and their relationships, are generally not very well known. Thus, at the moment the α-parameter can only be discussed in a qualitative fashion [71].

6 Summary of papers

In this section the main results of papers **I**-**V** are discussed. In addition, some aspects for future research are suggested.

6.1 Crystalline cellulose and nutrient elements in wood.

In paper **I**, secondary xylem (i.e. stem wood tissue) of Norway spruce was characterized using micro-focused x-ray synchrotron radiation. X-ray diffraction (XRD) was used to determine the average dimensions of cellulose crystallites (length L and width D), the fraction of oriented cellulose χ and the mean microfibril angle $\langle \mathrm{MFA} \rangle$, and x-ray fluorescence spectroscopy (XRF) was used to determine the content of atomic elements between atomic numbers 18 - 36 (i.e. from argon to krypton in the periodic table of elements). Unlike earlier similar x-ray studies on wood [36, 72], the XRD patterns and XRF spectra were simultaneously collected. The sample material was obtained from a well documented nutrient optimization field trial in Asa [73, 74], which is situated in southern Sweden. The tissue samples were taken from the 5th, 10th and 17th annual rings of a stem. Two separate samples were measured from each annual ring.

The results were processed at two levels. First, the ensemble of microscopic line scan points were used to estimate the variation of the measured quantities in the micrometer scale, i.e. within each annual ring. Second, averages of the micrometer scale results were calculated in order to compare the samples. The scatter of results within each sample and the average values of each sample as a function of cambial age are shown in Fig. 15.

The average dimensions of cellulose crystallites did not change as a function of the cambial age. The mean microfibril angle decreased from 12° in 5th annual ring to 7° in the 17th annual ring.

The scatter of microscopic results is mostly due to limited accuracy of the determination method, including the experimental setup and data analysis procedures. However, if this were the case, the scatter of results should be the about same in all the samples measured. As can be seen from Fig. 9 of paper **I**, the scatter of results seem to follow a trend. The variation in the diameter of cellulose crystallites is higher in the 5th annual ring than in the 10th or 17th rings. The behaviour is opposite in the case of the length of cellulose crystallites. The variation in the mean microfibril angle is higher in the 17th annual ring than in the 5th or 10th rings.

The XRF spectra were used for the determination of nutrient element content in the samples. All the spectra included characteristic peaks from elements Cl, Ar, K, Ca, Ti, Mn, Cu and Zn, from which the peaks of Ar, K, Ca, Mn and Zn were significant. The signal from argon was assumed to arise from the ambient atmosphere. The concentrations of potassium, calcium, zinc and manganese were determined.

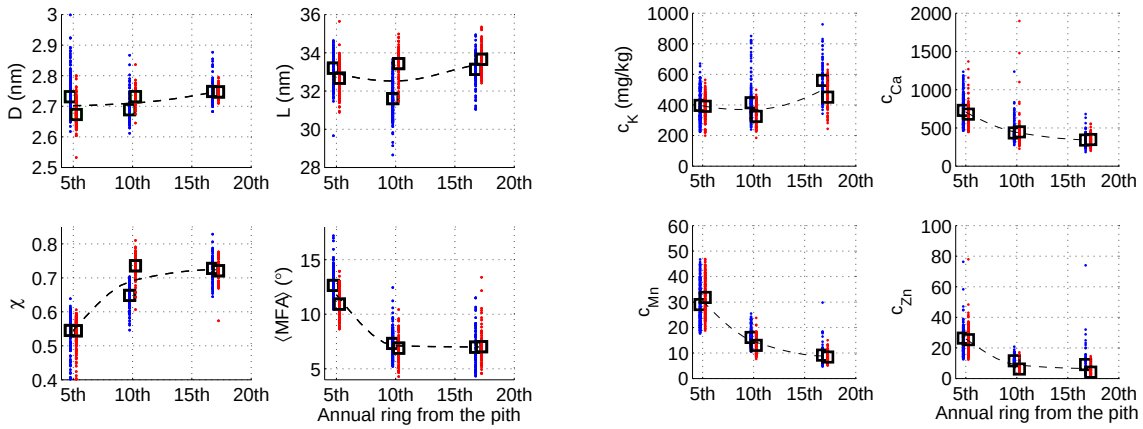

Figure 15: The results of x-ray microbeam line scans taken from stem wood of Norway spruce. Fig. a) shows the results from XRD and Fig. b) shows the results from XRF. Blue dots represent the 1st sample and red dots represent the 2nd sample. Black squares are expectation values from each sample. The dashed lines are spline interpolations, which follow the trend of the center of mass of the two mean values in each annual ring.

In general, the most abundant nutrient element was Ca, followed by K, Mn, Zn, and Cu in decreasing order. The mean concentration of K remained the same in the 5th and 10th rings, but increased in the 17th ring. The mean concentration of Ca, Mn and Zn decreased from the 5th to the 17th ring.

One of the important points in paper **I** is that when studying the macroscopic properties of wood, or similar biomaterials, the size of the probed volume-element can have a significant influence on the results. For example, in paper **I** a volume shaped as a rectangular prism with dimensions 15 μm x 75 μm x 1000 μm was scanned from each sample, and there were still significant differences in results between samples taken from the same annual ring of the same stem.

Perhaps the main problem in paper **I** is that the results apply only to one stem from the nutrient optimization experiment. Although the main idea of the paper was to comprehensively study the structural variation within one tree, the generalization of the results would require similar experiments on at least several stems from the same growth zone. Therefore, future research could include similar x-ray microanalysis experiments on statistically significant sample sets. One possibility is to experiment on stems from all the different growth plots in Asa, and compare the effect of different fertilisation schemes on the microstructural properties of cellulose and the nutrient element contents of wood.

The second problem is that longitudinal tracheids have actually been studied quite

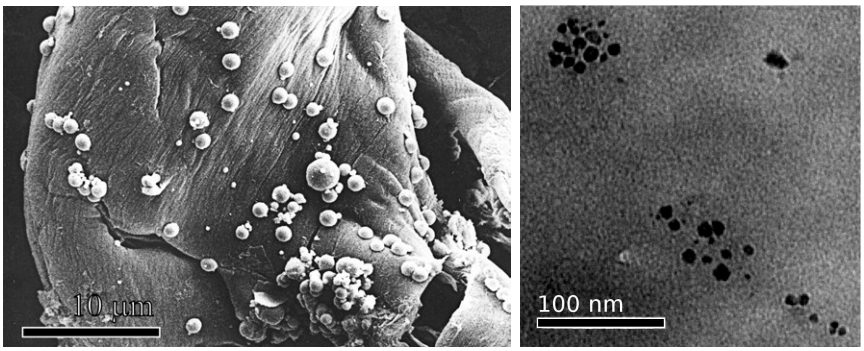

(a) (b)

Figure 16: Nanoparticles on the surface of cellulose fibers. Micrometer scale (Fig. a) is imaged with SEM and nanometer scale (Fig. b) is imaged with TEM.

comprehensively [35,36,75], so some of the results of paper **I** have already been known. However, the other cell types in the wood xylem have not received that much attention; for example, there are surprisingly few studies on the structure and properties of parenchyma cells. These cells are mainly found in rays that extend in the radial direction from the pith to the bark. The main function of these is considered to be the storage of nutrients.

Therefore it would be interesting to utilize x-ray microanalysis in the study of parenchyma cells to answer the following questions: What is the nanostructural arrangement of cellulose in ray parenchyma cells? How does the arrangement compare to the longitudinal tracheids? What is the distribution of nutrient elements in ray parenchyma cells? Is the model correct that they are mainly nutrient storages, or do they have some other function as well?

These studies could be complemented by microscopic techniques, such as optical microscopy (OM), scanning electron microscopy (SEM), and x-ray microtomography (μCT).

6.2 Cobalt nanoparticles in cellulose support

In paper **II**, cobalt containing nanoparticles in microcrystalline cellulose (MCC) matrix were studied by x-ray diffraction, x-ray absorption spectroscopy (XAS) and electron microscopy. These techniques were used to determine the effect of different chemical synthesis routes on the final structural properties of the nanoparticles. In addition, the magnetic properties of the nanoparticles were studied with a vibrating sample magnetometer (VSM).

In brief, cobalt containing nanoparticles were synthesized into the MCC matrix by diffusion of cobalt ions (Co^{2+}), and subsequent reduction of Co^{2+} into metallic cobalt

by using either borohydride (BH_4^-) or hypophosphite ($H_2PO_2^-$). The final samples were of fine powder consisting of about 5 to 10 mass% cobalt, the rest being cellulose.

X-ray diffraction and extended x-ray absorption fine structure (EXAFS) spectroscopy (at Co K-edge) were both used to study the atomic arrangement in the nanoparticles. However, in the case of poorly ordered particles XRD results are inconclusive whereas EXAFS is still useful in the determination of the average chemical neighborhood around Co-atoms. Scanning electron microscopy (SEM) was used to probe the micrometer size scale morphology of the samples, and transmission electron microscopy was used to study the surface of cellulose fibres at the nanometer size scale. Average magnetic properties of the powders were obtained from magnetic hysteresis curves measured by VSM.

In all the samples, spherical particles of various sizes were observed in pores or crevices on the surface of cellulose fibres. In some cases the particles were merged together to form larger aggregates (Fig. 16). The smallest observed particles were about 5-10 nanometers in diameter and the largest particles were 10 micrometers in diameter. According to XRD, the average crystallite size was between 6 to 15 nanometers.

Particles made via the $NaBH_4$ reduction were amorphous Co-B or Co oxide composites with diminished magnetic properties, and particles made via the NaH_2PO_2 reduction were well-ordered ferromagnetic hcp cobalt nanocrystals. The average crystalline arrangement of cellulose matrix did not change due to the making of the nanoparticles.

Although the actual nucleation and growth stage of the particles was not studied *in situ*, the growth mechanism is assumed to be following (see Fig. 17): A) the Co^{2+} ions diffuse into the MCC matrix, e.g. to the surfaces of cellulose fibers; B) the Co^{2+} is then chemically reduced to Co^0 (metallic cobalt). The nucleation begins on the grooves in the surface of cellulose fibres and small cobalt containing (single domain) nanocrystals are formed. At stage C) the nanocrystals join to form larger (multidomain) aggregate particles, which are gradually passivated by an oxide layer forming on the surfaces of the particles.

An interesting aspect is the large size dispersion of the particles. Why do some particles grow only to 10 nanometers whereas others grow to become 100 times larger? One possibility is that some of the particles grow in pores inside the cellulose fibres and the pores act as nanoreactors, controlling the maximum size of the nanoparticles. Also, the geometry of the grooves on the fiber surfaces could have an effect on the effective particle size. Unfortunately, the experiments done in paper **II** do not answer these questions. Instead, the effect of surface geometry on the growth of metallic nanocluster growth was studied with theoretical models and computer simulations in papers **IV** and **V**.

The next step would be to experimentally observe the growth of the particles *in situ*, using a combination of XRD, SAXS and possibly microscopic and spectroscopic techniques (see e.g. [13, 76]). One possibility would be to utilize the ID02 beamline

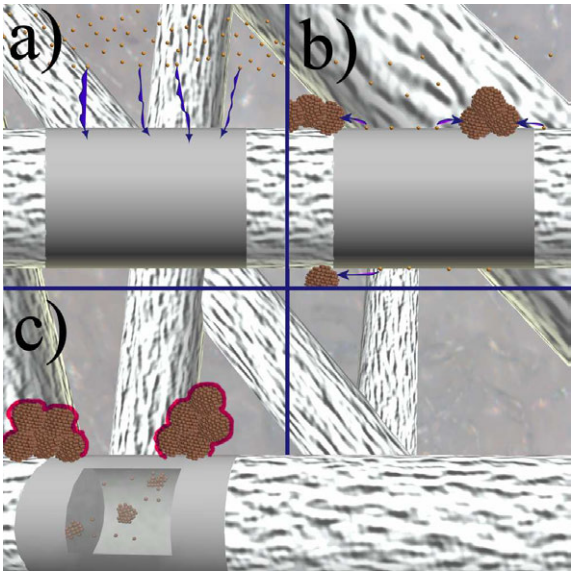

Figure 17: A scheme showing a) the diffusion of Co^{2+} into the MCC matrix, b) the nucleation of Co into spherical nanocrystals and the aggregation of these into larger multidomain particles. In c) the final multidomain particles are passivated by an oxide layer preventing further growth. Perhaps nanocrystals also grow inside the pores of cellulose fibers?

in ESRF, which can be used for WAXS, SAXS and USAXS (ultra small-angle x-ray scattering) experiments with a time resolution of milliseconds.

6.3 Average coordination number in nanocrystals

Many of the parameters used to characterize bulk matter have quite different values when applied to nanoscopic systems, e.g. interatomic distances and coordination numbers. The experimental methods most often used to obtain coordination numbers of a given material are x-ray diffraction (XRD) and extended x-ray absorption fine structure (EXAFS) spectroscopy. Quite often when EXAFS is used to characterize nanomaterials, the resulting low coordination numbers are explained arising from the experiment itself, or the data analysis involving fitting procedures with many correlated parameters. In paper **III**, it is emphasized that the average coordination numbers for perfectly crystalline spherical nanoparticles are significantly lower than the bulk values.

In paper **III**, the effect of very small crystal sizes on the average coordination number (ACN) was calculated. The following assumption were made:

1) The particles have a well defined crystal structure.

2) The interatomic distances are constant throughout the particle.

3) Crystals are free of defects.

4) The particle-particle distances are far enough to omit any interference effects i.e. there are no neighbouring particles within the fourth coordination shell radius from the surface of the particle.

The average coordination number was calculated in the case of spherical nanocrystals with simple cubic (SC), body-centered cubic (BCC), face-centered cubic (FCC) and hexagonal close-packed (HCP) lattices.

In very small crystals the ACN decreases down to 70-80% of the bulk value, the exact decrease depending on the type of lattice. Such a drop in the ACN can be detected e.g. with EXAFS. However, in the case of cobalt containing nanoparticles in paper **II**, the reduced ACN can not be reliably used for particle size analysis. This is because Co may undergo a phase transition from one structure to another when a critical particle size is reached. To complicate the situation further, in paper **II** there are larger compact particles in addition to nanosized particles. The larger micrometer sized particles dominate the EXAFS signal, thus making size estimation of the nanosized particles by coordination number analysis impossible.

Although paper **III** was written as a side study to the more experimental paper **II**, the primary applications for coordination number calculations may reside in more theoretical studies in which the size dependence of many physical properties of nanocrystals can be explained by the low coordination number of the surface atoms [77, 78].

Future studies on the subject include the calculation of coordination numbers for nanoislands (i.e. spherical caps) and surface coordination numbers (sCN) for spheres. Both cases would require only small modifications to the methods used in paper **III**.

6.4 Simulations on nucleation and growth of metallic nanoparticles

In paper **IV**, the size selected growth of metallic clusters was studied by theoretical models and computer simulations. The growth was described by rate equations, which includes only adatom attachment and detachment processes to the cluster edges. The time evolution of cluster size distributions was simulated by two fundamentally different computational schemes: the stochastic Particle Coalescence Method (PCM) and the deterministic direct numerical integration (Master Equation Discretization, MED) of the rate equations governing the growth. The results from these two schemes were compared with each other, and with analytic predictions of the underlying model.

The growth was modelled in two distinct stages: 1) the initial stage of growth and 2) the final stage where size selection occurs. In these stages of growth, it was possible to estimate the functional behaviour of the cluster size distributions by analytic solutions to the theoretical model.

In the initial stage of growth, the analytic prediction was that the size distribution is a streched exponential $n(s,t) \propto s^{-q}\exp(-F(s)/t)$ (see Sec. 3.3 of paper **IV**). The first test for the computational schemes was to reproduce the inverse power-law type behaviour at $t >> F(s)$. Both PCM and MED reproduced the correct singular distributions for $q = 0$, 1/4, 1/2, 3/4 and 1 (Fig. 18a).

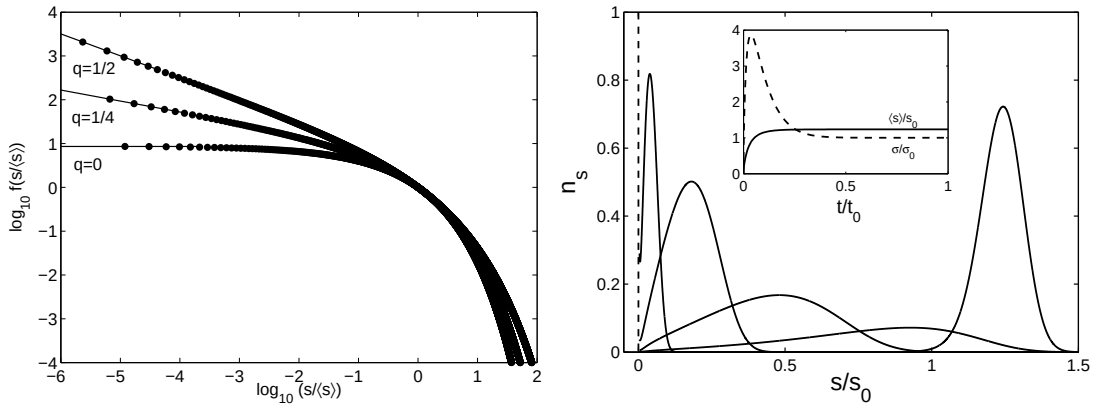

(a) (b)

Figure 18: The growth of nanoclusters on a flat surface as calculated by MED. Figure a) shows the initial growth in three different cases. Figure b) shows snapshots of the evolution towards the final stationary state.

In the late stages of growth, i.e. near the region where the size selection occurs, the analytic prediction is that the size distribution should be approximately Gaussian (see Sec. 3.4 of paper **IV**)

$$n(s,t) \propto \exp(\frac{s - \langle s(t) \rangle}{2\sigma(t)^2}),$$

with a time dependent peak position $\langle s(t) \rangle$ and a distribution width $\sigma(t)$. The final stationary value of peak position $s_c = \langle s(t \to \infty) \rangle$ cannot be obtained in analytical form, thus numerical calculations are required. Previous numerical studies [61] have shown that the size distribution overshoots the value s_0 (the cluster size at the free energy difference minimum) by a factor of 1.2-1.5.

According to both PCM and MED, in the intermediate stages of growth the size distribution begins to broaden (Fig. 18b). The main part of the size distribution is Gaussian and propagates rapidly to larger values, while the trailing edge is left behind and contains a large number of small clusters. Finally, the width of the size distribution begins to diminish and the size distribution attains a closely Gaussian shape and becomes stationary. It turns out both PCM and MED reproduce the final stationary size distribution in a similar way. In all the cases studied in paper **IV** the cluster size distribution overshot s_0 by a factor of 1.3. The stationary size distributions were Gaussian shaped but slightly skewed towards larger sizes.

In summary, it can be concluded that the narrowing of the size distribution in the stationary state is a very general feature of size selected growth of nanoclusters. In addition, the stationary position overshoots the thermodynamical energy minimum. The final stationary size distribution is a Gaussian with negative skewness. All these aspects were reproduced in a similar way by both computational schemes. Although the

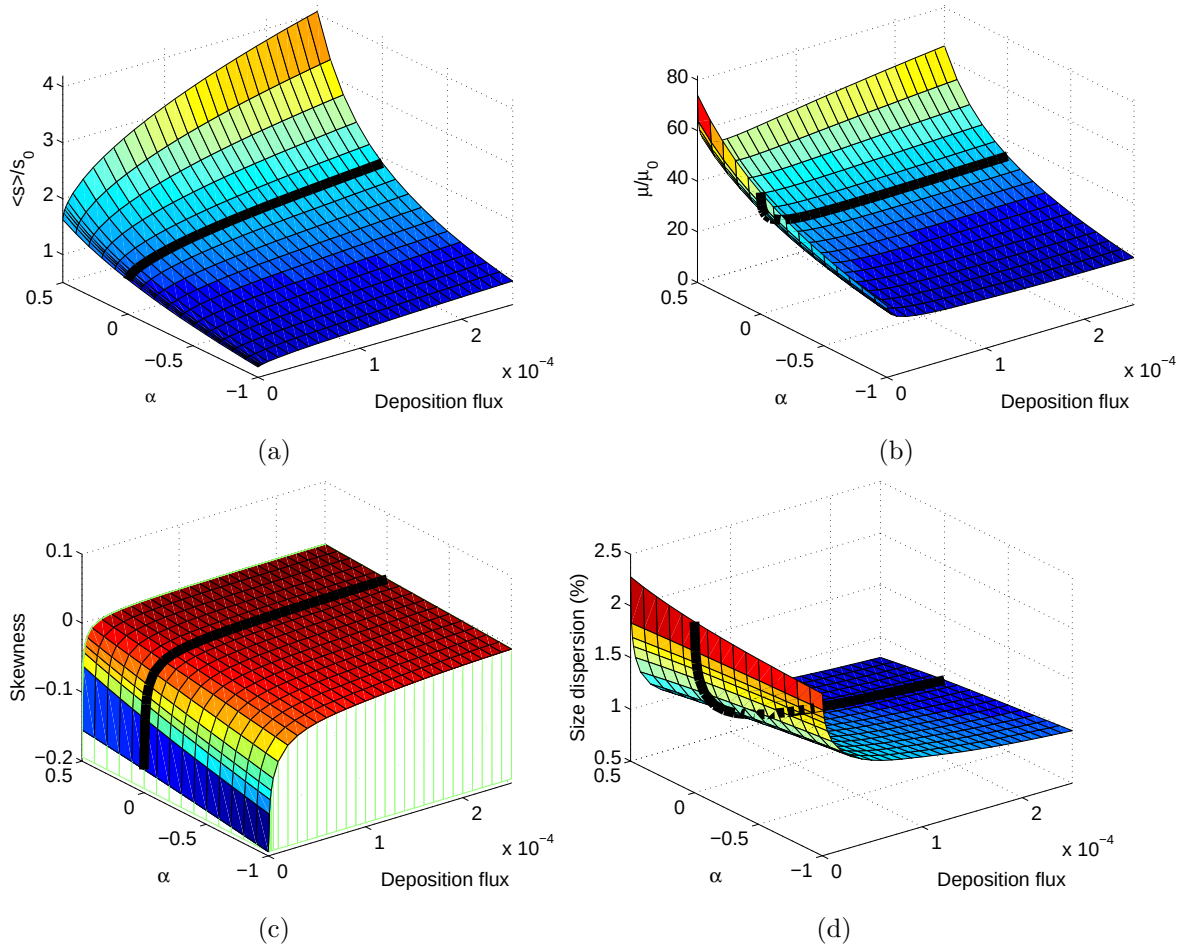

Figure 19: The properties of stationary cluster size distributions as a function of deposition flux and α-parameter. Fig. a) shows the stationary mean cluster size, Fig. b) shows the stationary size distribution width, Fig. c) shows the skewness i.e. the third moment of the stationary size distribution and Fig. d) shows the dispersion i.e. distribution width divided by the mean size.

schemes are quite efficient, the duration of a simulation from initial to the stationary state still took several days on a contemporary desktop computer. Due to the long simulation times the simulated parameter space was scarce.

In paper **V**, the effect of substrate geometry and deposition flux to the final stationary state was simulated by using a simplified version of the rate equations governing the growth. The computational scheme of choice was MED. The simplifications were done to speed up the calculations and made it possible to simulate the stationary state inside a larger parameter space.

The stationary cluster size distribution can be modified by the rate of adatom deposition and substrate geometry (Fig. 19). By tuning the values for the deposition flux and the geometric parameter α the mean size and width of the cluster size distribution

can be tailored to match needs. The skewness of the size distribution is also affected by the choice of these parameters, but the value for skewness quickly levels off to a nearly constant positive value. Smallest size dispersions can be acquired with positive values of α and higher deposition fluxes.

The results suggest that if the growth of metallic clusters proceeds on top of wedges with variable opening angles, the size distribution corresponding to the smallest clusters can shift to higher sizes by a factor of 2.1 (when no adatoms are deposited). Thus, this can be used to explain the size dispersion of nanosized cobalt containing particles in paper **II**, but it does not explain the existence of micron sized aggregates.

In many respects, paper **V** is only the first step in modelling growth of metallic clusters inside a biopolymer matrix. The growth on wedged surface is only a gross approximation of the true growth problem. In addition to the growth on the crevices on top of the cellulose fibrils, it is also possible that the growth takes place inside the porous fibrils. Furthermore, a more realistic model should at least take into account the surface morphology of the pores. At this time, however, the exact morphology or pore size distributions in microcrystalline cellulose is not known.

In the case that the nucleation of metallic clusters occurs inside the porous cellulose fibrils, a following experiment would in principle be possible to determine the pore size distribution:

1) The metallic clusters are prepared in the MCC matrix.

2) The clusters on the surface are somehow (e.g. chemically) removed.

3) The cluster size distribution is measured using anomalous small angle x-ray scattering (ASAXS) at the corresponding metal absorption edge.

4) An assumption is made that the cluster size distribution is approximately the same as the pore size distribution.

As it happens, an experiment including the items 1) and 3) has already been done for copper [25] and nickel [26] nanoparticles in MCC matrix. Item 2) would require a chemical treatment that would dissolve the clusters on surfaces of the cellulose fibrils, but would leave the fibrils itself mostly unaffected. Item 4) would require modelling of cluster growth inside closed pores. The main question would be: do the clusters fill the pores completely or only partially? Fortunately, the study of paper **V** already points out the direction to proceed in the modelling. Basically, no fundamental changes are probably needed, and what needs to be clarified or solved is the problem of how the parameter α is related to the different substrate morphologies and how the finite size and morphology of the pores affects the growth.

References

[1] R. Feynman, R. Leighton, and R. Sands, *The Feynman Lectures on Physics Vol. 1* (Addison-Wesley, Reading, 1964).

[2] D. Leslie-Pelecky and R. Rieke, Chem. Mater. **8**, 1770 (1996).

[3] *Nanoparticles From Theory to Application*, edited by G. Schmid (Wiley-VHC, Weinheim, 2004).

[4] B. Cullity and S. Stock, *Elements of x-ray diffraction* (Prentice Hall, New Jersey, 2001).

[5] J. Watson and F. Crick, Nature **171**, 737 (1953).

[6] C. Bunn, Trans. Faraday Soc. **35**, 482 (1939).

[7] M. Bevis and E. Crellin, Polymer **12**, 666 (1971).

[8] P. Zugenmaier, Prog. Polym. Sci. **26**, 1341 (2001).

[9] G. Schmid, Chem. Rev. **92**, 1709 (1992).

[10] K. Klabunde *et al.*, J. Phys. Chem. **100**, 12142 (1996).

[11] H. Gleiter, Nanostruct. Mater. **6**, 3 (1995).

[12] H. Gleiter, Acta Mater. **48**, 1 (2000).

[13] M. Andersson, J. Pedersen, and A. Palmqvist, Langmuir **21**, 11387 (2005).

[14] *Magnetic Nanoparticles*, edited by S. Gubin (Wiley-VHC, Weinheim, 2009).

[15] G. Binasch, P. Grünberg, F. Saurenbach, and W. Zinn, Phys. Rev. B **39**, 4828 (1989).

[16] M. Baibich *et al.*, Phys. Rev. Lett. **61**, 2472 (1988).

[17] A. Guinier, *X-ray diffraction in crystals, imperfect crystals and amorphous bodies* (Dover publications, New York, 1994).

[18] J. Als-Nielsen and D. McMorrow, *Elements of modern x-ray physics* (Wiley, New York, 2004).

[19] D. Dinega and M. Bawendi, Angew. Chem. Int. Ed. **38**, 1788 (1999).

[20] V. Puntes, K. Krishnan, and A. Alivisatos, Top. Catal. **19**, 145 (2002).

[21] G. Cheng, J. Carter, and T. Guo, Chem. Phys. Lett. **400**, 122 (2004).

[22] C. Yang, J. Cryst. Growth **47**, 274 (1979).

[23] L. Marks, Rep. Prog. Phys. **57**, 1994 (1994).

[24] B. Hall, J. Appl. Phys. **87**, 1666 (2000).

[25] U. Vainio *et al.*, Eur. Phys. J D **42**, 93 (2007).

[26] K. Pirkkalainen *et al.*, J. Appl. Cryst. **40**, s489 (2007).

[27] E. Sjöström, *Wood chemistry fundamentals and applications* (Academic press, San Diego, 1993).

[28] D. Klemm, H.-P. Schmauder, and T. Heinze, in *Biopolymers*, edited by A. Steinbüchel (Wiley-VHC, Weinheim, 2003), Vol. 6, Chap. 10.

[29] E. Kontturi *et al.*, Biomacromolecules **12**, 770 (2011).

[30] J. Sugiyama, R. Vuong, and H. Chanzy, Macromolecules **24**, 4168 (1991).

[31] Y. Nishiyama, P. Langan, and H. Chanzy, J. Am. Chem. Soc. **124**, 9074 (2002).

[32] H. Lichtenegger, A. Reiterer, S. Stanzl-Tschegg, and P. Fratzl, J. Struct. Biol. **128**, 257 (1999).

[33] H. Lichtenegger, M. Müller, R. Wimmer, and P. Fratzl, Holzforschung **57**, 13 (2003).

[34] M. Eder, K. Jungnikl, and I. Burgert, Trees - Structure and function **23**, 79 (2009).

[35] M.-P. Sarén, Ph.D. thesis, University of Helsinki, 2006, `http://urn.fi/URN:ISBN:952-10-2110-1`.

[36] M. Peura, Ph.D. thesis, University of Helsinki, 2007, `http://urn.fi/URN:ISBN:978-952-10-3258-5`.

[37] L. Salmén and I. Burgert, Holzforschung **63**, 121 (2009).

[38] S. Andersson *et al.*, J. Wood Sci. **49**, 531 (2003).

[39] M. Peura *et al.*, Trees - Structure and function **22**, 49 (2008).

[40] G. Arfken and H. Weber, *Mathematical methods for physicists* (Harcourt academic press, San Diego, 2001).

[41] *International tables for crystallography Vol. C*, edited by A. Wilson and E. Prince (Kluwer Academic Publishers, Dordrecht, 1999).

[42] P. Fuoss, P. Eisenberger, W. Warburton, and A. Bienenstock, Phys. Rev. Lett. **46**, 1537 (1981).

[43] J. Simon and O. Lyon, *Resonant Anomalous X-ray Scattering* (Elsevier Science, Amsterdam, 1994).

[44] W. Kraus and G. Nolze, J. Appl. Cryst. **29**, 301 (1996).

[45] I. Bruno *et al.*, Acta Crystallogr., Sect. B: Struct. Sci **58**, 389 (2002).

[46] M. Sarén *et al.*, J. Struct. Biol. **136**, 101 (2001).

[47] H. Jakob, P. Fratzl, and S. Tschegg, J. Struct. Biol. **113**, 13 (1994).

[48] I. Cave, For. Prod. Jour. **16**, 37 (1966).

[49] S. Verrill, D. Kretschmann, and V. Herian, *JMFA - A graphically interactive Java program that fits microfibril angle X-ray diffraction data. Reseach Note FPL-RN-0283*, Madison, WI: U.S. Department of Agriculture, Forest Service, Forest Products Laboratory., 2001, `http://www.fpl.fs.fed.us/documnts/fplrn/fplrn283.pdf`.

[50] B. Teo, *EXAFS: basic principles and data analysis* (Springer-Verlag, Berlin, 1986).

[51] *Characterization of nanophase materials*, edited by Z. Wang (Wiley-VHC, Weinheim, 2000).

[52] D. Bazin, D. Sayers, and J. Rehr, J. Phys. Chem. B **101**, 11040 (1997).

[53] H. Modrow, Appl. Spect. Rev. **39**, 183 (2004).

[54] J. Rehr and R. Albers, Rev. Mod. Phys. **72**, 621 (2000).

[55] V. Honkimäki, K. Hämäläinen, and S. Manninen, X-ray spectrom. **25**, 215 (1996).

[56] M. Bielewski *et al.*, X-ray Spectrom. **35**, 238 (2006).

[57] V. Solé *et al.*, Spectrochim. Acta Part B **62**, 63 (2007).

[58] F. Liu, A. Li, and M. Lagally, Phys. Rev. Lett. **87**, 126103 (2001).

[59] Z. Gai *et al.*, Phys. Rev. Lett. **89**, 235502 (2002).

[60] D. Jesson, T. Munt, V. Shchukin, and D. Bimberg, Phys. Rev. Lett. **92**, 115503 (2004).

[61] K. Nevalainen, M. Rusanen, and I. Koponen, Eur. Phys. J. B **56**, 311 (2007).

[62] R. Becker and W. Döring, Ann. Phys. **4**, 719 (1935).

[63] V. Slezov and J. Schmelzer, J. Phys. Chem. Solids **59**, 1507 (1998).

[64] J. Neu and L. Bonilla, *Kinetic theory of nucleation and coarsening*, 2006, `arXiv:cond-mat/0603330v1`.

[65] F. Mandl, *Statistical physics* (Wiley, Chichester, 1988).

[66] R. Chang, *Physical chemistry for the chemical and biological science* (University Science Books, Sausalito, California, 2000).

[67] R. Alberty, J. Chem. Educ. **81**, 1206 (2004).

[68] G. Bales and A. Zangwill, Phys. Rev. B **55**, R1973 (1997).

[69] F. Liu, Phys. Rev. Lett. **89**, 246105 (2002).

[70] C. Sholl and N. Fletcher, Acta Metall. **18**, 1083 (1970).

[71] V. Shchukin and D. Bimberg, Rev. Mod. Phys. **71**, 1125 (1999).

[72] M. Peura *et al.*, Trees - Structure and function **22**, 499 (2008).

[73] J. Bergh, S. Linder, T. Lundmark, and B. Elfving, For. Ecol. Manage. **119**, 51 (1999).

[74] J. Bergh, S. Linder, and J. Bergström, For. Ecol. Manage. **204**, 1 (2005).

[75] S. Andersson, Ph.D. thesis, University of Helsinki, 2006, `http://urn.fi/URN:ISBN:952-10-3235-9`.

[76] C. Tyrsted *et al.*, Chem. Mater. **22**, 1814 (2010).

[77] R. Benfield, J. Chem. Soc. Faraday Trans. **88**, 1107 (1992).

[78] M. Shandiz, J. Phys.: Condens. Matter **20**, 325237 (2008).